



Erasmus Mundus Master
in Astrophysics and Space Science

Master Thesis

Data reduction and modelling of dust emissions in
three nearby Active galactic Nuclei.

Supervisors

Dr Dragana Ilić
Physics Dept., University of Belgrade

Dr Marko Stalevski
Astronomical Observatory, Belgrade

Dr James Leftley
Observatoire de la Côte d'Azur

Author

Josiah Olumuyiwa Faniyi

Academic Year 2023/2024



UNIVERZITET U BEOGRADU
MATEMATIČKI FAKULTET



Josiah O. Faniyi

DATA REDUCTION AND MODELLING OF DUST EMISSIONS IN
THREE NEARBY ACTIVE GALACTIC NUCLEI

master rad

Beograd, 2024.

Supervisor:

dr Dragana ILIĆ, Associate Professor
University of Belgrade, Faculty of Mathematics

Committee Members:

dr Marko STALEVSKI, Associate Research Professor
Astronomical Observatory, Belgrade

dr James LEFTLEY,
Université Cote d'Azur, Nice, France

dr Luka POPOVIĆ, Full Professor
University of Belgrade, Faculty of Mathematics

dr Francesco Tombesi, Associate Professor
University of Rome, Tor Vergata, Physics Department

Defense Date: _____

This Master thesis is submitted in partial fulfilment of the requirements for the degree "MASTER ASTROFIZICAR" as part of a multiple degree awarded in the framework of the Erasmus Mundus Joint Master in Astrophysics and Space Science – MASS jointly delivered by a Consortium of four Universities: Tor Vergata University of Rome, University of Belgrade, University of Bremen, and Université Cote d'Azur, regulated by the MASS Consortium Agreement and funded by the EU under the call ERASMUS-EDU-2021-PEX-EMJM-MOB.

Contents

Contents	iv
Acknowledgements	1
Abstract	3
1 Chapter 1 - Introduction	4
1.1 AGN structure	5
1.2 AGN types and Classifications	5
1.2.1 Type-I AGNs	6
1.2.2 Narrow Emission Lines in Type-I AGNs	7
1.2.3 High-Luminosity Type-I AGNs	7
1.2.4 Type-II AGNs	7
1.2.5 Significance of Narrow-Line Region Studies	8
1.3 AGN Unification Model and Structure	9
1.3.1 Evidence Supporting the Unification Model	10
1.3.2 Advances in the Unification Model	10
1.4 The Dusty Torus	11
1.5 Dust in the Polar Region and Dusty Winds	12
1.6 Goals and Structure of the thesis	13
2 Chapter 2 - Observations	14
2.1 Sample Selection and Instrumentation	14
2.1.1 ESO 323-G77	14
2.1.2 ESO 428-14	15
2.1.3 NGC 5506	15
3 Chapter 3 - Data Reduction	17
3.1 IMAGE REDUCTION WORKFLOW	17
3.2 SPECTROSCOPY WORKFLOW	19
3.3 Python Script	19
4 Chapter 4 - Methods	22
4.1 Monte Carlo Radiative Transfer	22
4.2 SKIRT Code	23
4.3 MODELS	24
4.3.1 SKIRTOR	24
4.4 CIGALE	26

5 Chapter 5 - Results and Discussions	29
5.1 ESO 323-77	29
5.2 ESO 428-14	33
5.3 NGC 5506	33
Summary	46
References	53
Appendix	54
Biography	66

Acknowledgements

First, I express my deep gratitude to my supervisors, Dr. Marko Stalevski and Dr. James Leftley, for their incredible support and mentorship throughout the course of this project. I appreciate the entire faculty of all the consortium universities at MASS for the knowledge imparted and the experiences shared.

I am also grateful to all my colleagues in this program across the consortium universities for the two-year journey that is now coming to an end. I appreciate that we could come together, discuss, and support one another when the going got tough.

A heartfelt thank you to Dr. Médéric Boquien and Dr. Guang Yang for answering my questions when I encountered problems using CIGALE. I also extend my thanks to my colleagues, Aman Raju and Aurello Deandrea, for their help in debugging my Python script.

It has been two years since I left home, and I am deeply thankful for the prayers and moral support I have received from my parents, Ojo and Omolara Faniyi. To my loving siblings, Grace, Glory, Gideon, Eunice, and Esther—thank you for understanding your big brother.

Finally, to all the friends and more-than-friends I met along the way, I cannot be grateful enough for our paths crossing. Thank you!

Josiah Olumuyiwa Faniyi acknowledges support through an Erasmus Mundus Joint Master (EMJM) scholarship funded by the European Union in the framework of the Erasmus+, Erasmus Mundus Joint Master in Astrophysics and Space Science – MASS. Views and opinions expressed are however those of the author(s) only and do not necessarily reflect those of the European Union or the granting authority European Education and Culture Executive Agency (EACEA). Neither the European Union nor the granting authority can be held responsible for them.

Abstract

The aim of this thesis is to characterize the dusty wind in AGN samples by processing and modelling the infrared spectro-photometric observations of three objects from the AGN sample in which the existence of dust in the polar region was established: ESO 323-G77, ESO 428-14, NGC 5506. Both archival and new, previously unpublished observations from the VLT telescope at the Paranal Observatory in Chile are included. For modelling, the classic dust torus model is used as well as a new model, which includes the disk, and dusty winds in the form of a hollow cone in the polar region. The publicly available code CIGALE is used for fitting. As the main result, the parameters of the geometry and physical properties of the dust is determined. This is the first step towards characterising the dusty winds of a larger sample of AGNs, with the aim of establishing the conditions under which they arise and how they affect the galaxies in which they are located.

1 Chapter 1 - Introduction

Active galactic nuclei (AGN) are extremely energetic astrophysical sources that derive their power from the process of accretion onto supermassive black holes (SMBH) located at the center of galaxies (Netzer (2013) Peterson (1997)). These AGNs exhibit distinct observational characteristics that span the entire electromagnetic spectrum, encompassing a wide range of frequencies spanning more than twenty orders of magnitude (Netzer (2013)). The study of AGNs is crucial to gaining insights into the formation and evolution of galaxies (Peterson (1997)).

AGNs interact with gases in their host galaxy through radiation pressure, winds and jets. The energy output from AGNs, driven by the accretion of matter onto the supermassive black holes (SMBH) at their centers, can profoundly influence both the interstellar medium and the intergalactic medium (Fabian (2012)).

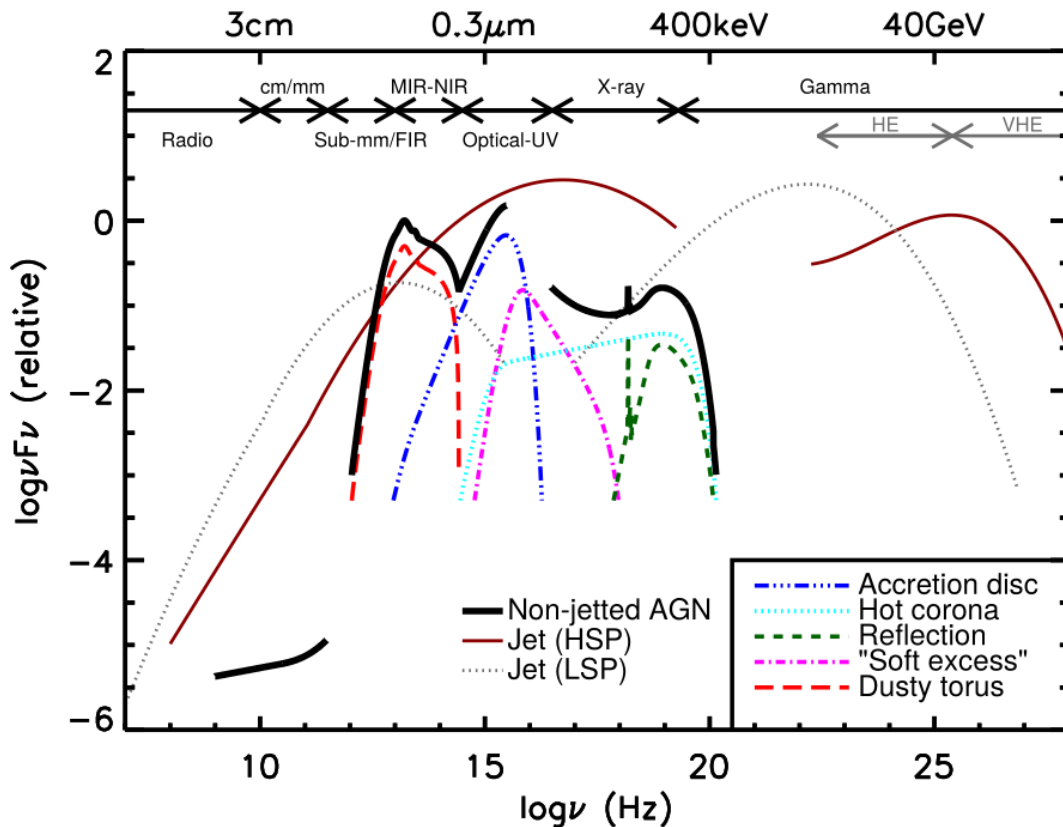


Figure 1: A schematic representation of an AGN spectral energy distribution (SED). Image credit: Harrison (2017)

1.1 AGN structure

There are many different structures in a typical AGN. Every AGN has a driving engine at its centre which is the SMBH. It is the primary source of gravitational energy, and it creates an accretion disk around itself, responsible for the UV/optical continuum. In the accretion disk, matter is funneled into the supermassive black hole and it is surrounded by a cloud of high-density gas moving at high speeds and consequently emitting broad optical/UV lines. This is the Broad line region (BLR) (Peterson (1997)). Reverberation mapping studies have shown that the inner radius of this region scales with luminosity and is $\sim 10 - 100$ light days (Peterson (1997)).

The AGN also has a narrow line region, located at 100-300 parsec, where narrow optical lines are created, and a dusty molecular “torus”, a few parsecs from the SMBH (Antonucci (1993), Urry and Padovani (1995)). The NLR contains dust, except for the innermost regions, known as the coronal line region, where high-ionization lines are produced. This region is relatively free of dust due to the intense radiation from the central AGN, which can sublimate dust grains (Netzer (2013)). The ionization cones are shaped by the interaction between the AGN’s radiation and the surrounding interstellar medium, creating a conical structure of ionized gas that extends outward from the AGN (Krolik (1999)). These cones are often observed in imaging studies, revealing the impact of the AGN on its host galaxy (Mulchaey et al. (1996), Davies et al. (2020)). Nuclear IR emission is associated with the presence of obscuring material and dust in the parsec scale vicinity of the SMBH (Netzer (2013)). This obscuring material is toroidal in shape in the classical AGN unification. It contains cold dust and gas, and obscures the central source from certain viewing angles, leading to the classification of AGNs into Type-1 and Type-2 in Antonucci (1993). Near-infrared reverberation studies have shown that the inner radius of the torus scales with luminosity Netzer (2013)).

There has been observations of polar dust structures in some AGNs, this interacts with outflows from the AGN and contributes to the infrared emission. Existence of polar dust gives new insights about the existing models of AGN dust (see 1.5).

1.2 AGN types and Classifications

There are several subtypes of AGN based on their observational characteristics and the wavelength regime in which they are observed. Table 1 in Padovani (2017) (see Table 4) provides a possibly non-exhaustive list of the different kinds of AGN, including Quasars, Seyfert 1s and Seyfert 2s, Quasi-stellar objects, Radio quiet and Radio Loud AGNs, Jetted and non-jetted, Type-I and Type-II, Farnoff-Riley class I and II radio sources, BL Lacertae objects, and Blazars. Most AGNs are radio-quiet and can be divided into

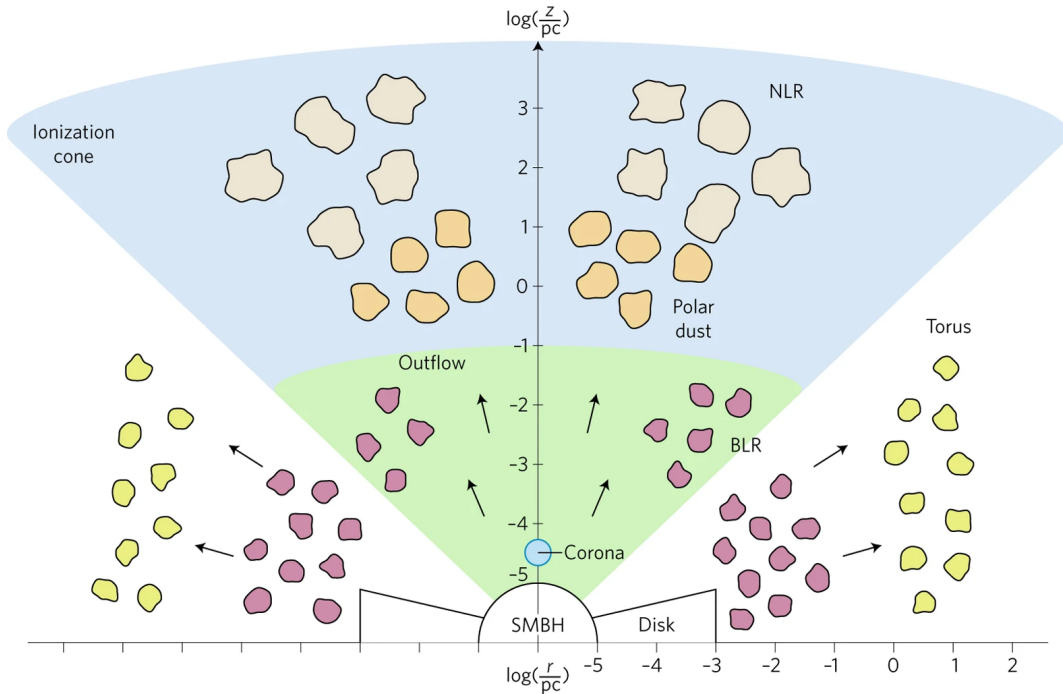


Figure 2: Sketch of the main AGN structures seen along the equatorial and polar direction. From the center to host-galaxy scales: SMBH, accretion disk and corona, BLR, torus and NLR. Different colours indicate different compositions or densities. (Figure 1 Ricci et al. (2017))

two classes according to their optical spectra. Type-I AGNs, also called Seyfert 1s (Sy1s), show both broad and narrow lines, while Type-II AGNs (Seyfert 2s or Sy2s) show only narrow lines (Antonucci, 1993Antonucci (1993)). In other words, Type-1 AGNs are unobscured, while Type-2 AGNs are obscured.

1.2.1 Type-I AGNs

The spectra of Type-I AGNs are distinguished by the optical and ultraviolet (UV) continuum emission dominated by the radiation from the accretion disk surrounding the SMBH. This continuum emission can be described by a power-law spectrum. And by broad emission lines with full-width at half-maximum (FWHM) velocities greater than or equal to 1000km/s . These broad lines arise from the broad-line region (BLR) within the AGN, which consists of high-density, dust-free gas clouds. These clouds are situated at a luminosity-dependent distance of approximately 0.01 to 1 parsec from the central black hole and move at velocities consistent with Keplerian orbits around the black hole (Peterson (1997)). The BLR is a critical region for understanding the dynamics and physical conditions close to the AGN's central engine, as it provides direct evidence of the high-velocity gas in the immediate vicinity of the supermassive

black hole (Sulentic et al. (2000), Netzer (2015)).

1.2.2 Narrow Emission Lines in Type-I AGNs

Many low- to intermediate-luminosity Type-I AGNs exhibit pronounced high-ionization narrow emission lines, including forbidden lines such as [O III] and [N II]. These emission lines originate from the narrow-line region (NLR), located further out from the black hole than the BLR and contains lower-density gas. The presence of these high-ionization lines indicates strong photoionization by the AGN's central source, and these sources are commonly referred to in the literature as Seyfert 1 galaxies or Quasi-Stellar Objects (QSOs) (Osterbrock and Ferland (2006), Kewley and Nicholls (2019)). Seyfert 1 galaxies are a subset of Type-I AGNs that are generally lower in luminosity than QSOs but share similar spectral characteristics (Khachikian and Weedman (1974)).

1.2.3 High-Luminosity Type-I AGNs

In contrast, high-luminosity Type-I AGNs often lack these narrow emission lines in their spectra. This absence can be attributed to the intense radiation field produced by the central engine, which ionizes the surrounding gas to such an extent that the conditions necessary for forming narrow forbidden lines are not met (Netzer (2013)). The higher luminosity in these AGNs results in a more significant photoionization effect, which either ionizes the gas completely or pushes the NLR to much larger distances where the density of gas drops and becomes less detectable (Krolik (1999)). Understanding the differences in emission line spectra among Type-I AGNs provides valuable insights into the physical processes occurring near the central black hole and the interactions between the AGN and its host galaxy. The study of these emission lines, both broad and narrow, helps to elucidate the structure of the AGN, the dynamics of the gas in different regions, and the impact of the AGN's radiation on its immediate environment (Fabian (2012), Heckman and Best (2014)).

1.2.4 Type-II AGNs

Type-II AGNs, are characterized by strong, narrow emission lines with FWHM velocities between 300 to 1000 km/s . These lines originate from the NLR, situated further away from the central black hole and the obscuring dusty torus. The NLR consists of lower-density, lower-velocity ionized gas that extends in the general direction of the ionization cones, reaching distances up to hundreds and even thousands of parsecs from the central engine (Antonucci (1993), Urry and Padovani (1995)).

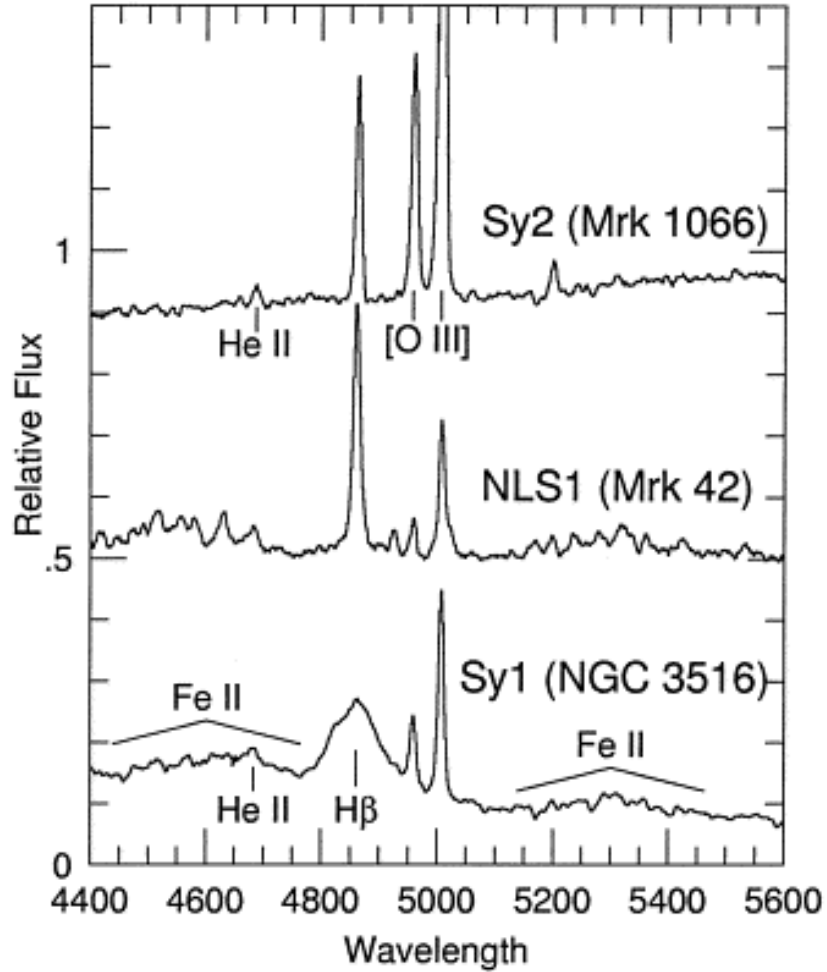


Figure 3: Spectra in the wavelength region of $H\beta$ of the NLS1 Mrk 42 (center), the Sy1 NGC 3516 (below), and the Sy2 Mrk 1066 (above). (From Pooge (2000))

1.2.5 Significance of Narrow-Line Region Studies

The NLR's lower-density and lower-velocity gas contrasts with the BLR found in Type-I AGNs, which is closer to the central black hole and thus exhibits higher velocity dispersions. The properties of the NLR in Type-II AGNs provide crucial insights into the physical conditions and dynamics of the gas in the vicinity of AGNs. Understanding the NLR helps astronomers probe the interaction between AGNs and their host galaxies, shedding light on the mechanisms of AGN feedback and its influence on galaxy evolution (Peterson (1997), Osterbrock and Ferland (2006)). Type-II AGNs, through their distinctive observational characteristics, offer a unique perspective on the nature of AGNs and their role in the broader context of galaxy formation and evolution. By studying the narrow emission lines and the structure of the NLR, researchers can gain a deeper understanding of the physical processes occurring in these enigmatic and pow-

erful sources of cosmic energy (Fabian (2012), Harrison (2017)).

1.3 AGN Unification Model and Structure

According to the simple unification model, all Type-I and Type-II AGNs are intrinsically the same but are observed with different inclination angles with respect to the molecular torus. Type-I AGNs are observed pole-on, allowing visibility of both the BLR and the NLR, while Type-II AGNs are seen edge-on, hiding the BLR behind the torus. The model assumes that all AGNs have the same intrinsic structure, including a central supermassive black hole, an accretion disk, a BLR, an NLR, and a dusty torus. (Antonucci, 1993; Urry and Padovani, 1995)

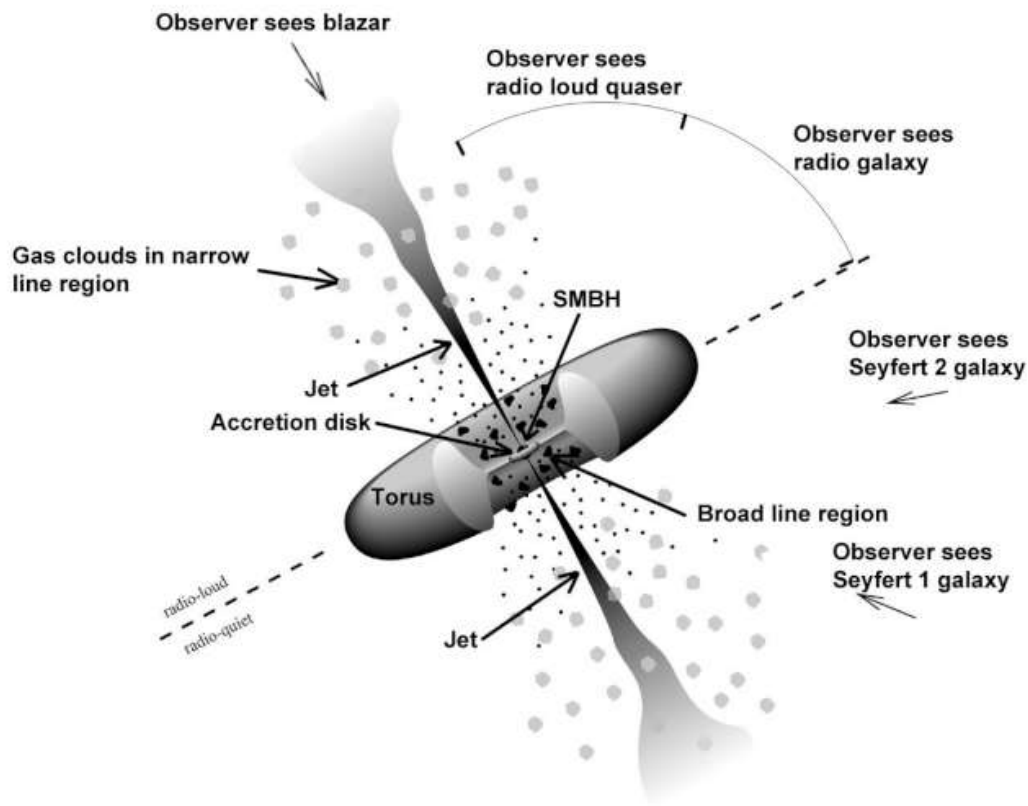


Figure 4: The AGN unification structure (Credit: J. D Meyers from <https://fermi.gsfc.nasa.gov/science/eteu/agn/>)

The observed differences are attributed to orientation effects rather than intrinsic differences among AGNs. Additionally, the radiation from the central engine is anisotropic, with the dusty torus absorbing and re-emitting this radiation, contributing to the anisotropy (Krolik (1999)). The BLR, located closer to the supermassive black hole, produces broad emission lines due to the high velocity of gas in this region, while

the NLR, located further out, produces narrow emission lines due to the lower velocity of gas. The visibility of these regions depends on orientation and torus obscuration (Netzer (2013)).

The model posits that the size of the BLR and the inner edge of the torus scale with the luminosity of the AGN, supported by reverberation mapping studies showing a correlation between the variability of the AGN’s light and the size of these regions (Peterson (1997); Netzer (2013)).

Seyfert 1 galaxies and quasars are viewed at small angles to the line of sight, allowing an unobscured view of the BLR and central engine, leading to the observation of both broad and narrow emission lines. In contrast, Seyfert 2 galaxies and radio galaxies are viewed edge-on, with the dusty torus blocking the direct view of the BLR and central engine, resulting in the observation of only narrow emission lines from the NLR (Antonucci (1993); Urry and Padovani (1995)).

1.3.1 Evidence Supporting the Unification Model

Polarimetric observations have revealed hidden BLRs in some Seyfert 2 galaxies through scattered light, supporting this orientation-based model (Tran (2001); Ramos Almeida and Ricci (2017)). Infrared observations detect thermal emission from the dusty torus in both Type-I and Type-II AGNs, suggesting similar structures across different AGN types (Lusso et al. (2013); Lyu and Rieke (2018)). X-ray observations show that Type-II AGNs exhibit significant absorption due to obscuring material, while Type-I AGNs have relatively unobstructed views (Risaliti et al. (2009)). These findings align with the unification model’s prediction that the orientation of the dusty torus significantly impacts the observed properties of AGNs.

1.3.2 Advances in the Unification Model

Recent studies have advanced the unification model by incorporating the effects of AGN feedback on the host galaxy and the role of the environment in shaping AGN properties. High-resolution observations have revealed complex structures in the dusty torus, including clumpiness and warping, influencing anisotropic emission and the degree of obscuration (Ramos Almeida et al. (2011); Laha and Ghosh (2020)). Simulations show that the interaction between AGN outflows and the host galaxy’s interstellar medium can impact the morphology and dynamics of the dusty torus, leading to variations in the observed properties of AGNs over time (Wada (2015); Hopkins et al. (2016)). Antonucci’s unification model provides a comprehensive framework for understanding the various observational characteristics of AGNs by accounting for orientation effects caused by the dusty torus. Continued refinement and validation through multiwave-

length observations and theoretical advancements underscore its significance in the study of AGNs and their role in galaxy evolution.

1.4 The Dusty Torus

The dusty torus in the unification model of radio-quiet Type-I and Type-II AGNs plays a significant role in the absorption and re-emission of radiation from the central source in the infrared spectrum. It connects the host galaxy to the accreting black hole, feeds the black hole, and provides important information about the feedback that the black hole gives to the host galaxy. Since the first straw person model of the torus presented by Antonucci (1993), many studies have aimed to understand the composition, structure, and dynamics of the torus and how they affect observational characteristics. The circumnuclear material is complex, clumpy, and dynamic, with its covering factor depending on the accretion properties of the AGN (Stalevski et al. (2016)). From the infrared point of view, this obscuring material represents a transition zone between the broad- and narrow-line regions and, in at least some galaxies, consists of two structures: an equatorial disk/torus and a polar component (Ramos Almeida and Ricci (2017)). The torus is not a homogenous structure; it is composed of numerous dusty clouds that can move and change, influenced by the AGN's radiation and other internal processes (Elitzur (2012)).

Studies using infrared interferometry have provided direct evidence of the clumpy nature of the torus, revealing that the dust distribution is not smooth but rather consists of discrete clouds with varying densities and temperatures (Jaffe et al. (2004); Tristram et al. (2007)). This clumpy structure impacts the amount of radiation that can escape or be re-emitted in different directions, thus influencing the observed spectral energy distribution (SED) of the AGN (Nenkova et al. (2008)).

The dynamics of the torus are also influenced by interactions with the accretion disk and the broad-line region (BLR). The interplay between radiation pressure from the AGN, gravitational forces, and other feedback mechanisms can lead to significant changes in the structure and distribution of the dusty clouds over time (Hönig and Beckert (2007)). This dynamical behavior of the torus is crucial for understanding the time variability seen in AGNs, such as changes in their infrared emission and the obscuration of the central engine (Ramos Almeida and Ricci (2017)).

Furthermore, the covering factor of the torus, which is the fraction of the sky as seen from the central black hole covered by the torus, varies with the luminosity and accretion rate of the AGN. High-accretion rate AGNs tend to have a smaller covering factor, meaning less of the central engine is obscured, which can affect the observed properties of the AGN (Lawrence (1991); Ricci et al. (2017); Stalevski et al. (2016)). Understand-

ing the covering factor helps in interpreting the diversity of AGN observations and the relationship between Type-I and Type-II AGNs.

1.5 Dust in the Polar Region and Dusty Winds

The discovery of dust in the polar regions and the presence of dusty winds challenge the traditional view of the torus as solely an equatorial structure. Mid-infrared (MIR) interferometry with the Very Large Telescope Interferometer (VLTI)/MIDI of 23 AGNs revealed that a large part of the MIR flux is concentrated on scales between 0.1-10 parsecs. For most of these galaxies, a two-component model is needed to explain the observations instead of a single toroidal structure. Polar dust emission has been detected in several AGNs over the past decade, indicating that dust can also be present in outflows along the polar direction, possibly driven by radiation pressure from the AGN (Hönig (2019); Asmus et al. (2016); Asmus (2019)).

Evidence for this diffuse MIR-emitting polar component has been found in an increasing number of galaxies, including NGC 5506, ESO 323 (Leftley et al. (2018)), ESO 428, Circinus (Stalevski et al. (2017, 2019); Stalevski et al. (2023)), NGC 424 (Hönig et al. (2012), NGC 1068, and NGC 3783 (Hönig et al. (2013)). This polar component was first discovered in NGC 1068 using high angular resolution MIR observations ($\leq 0.5''$) with single-dish 4-10m class telescopes. In the study of NGC 1068, it was found that 60-70 % of the 8-24.5 micron emissions were produced by dust in ionization cones. Similar results were observed for 18 active galaxies observed with 8m class telescopes in the MIR. The resolved emission is elongated in the polar direction, corresponding to the narrow-line region (NLR) dust, and represents about 40% of the MIR flux, scaling with the [O IV] flux. This is consistent with results from MIR interferometry, with the primary difference being the scales of the IR-emitting regions probed (Ramos Almeida and Ricci (2017)). Stalevski et al. (2017, 2019) modeled the Circinus galaxy using both the traditional torus model and their new disk-plus-wind model. Their results demonstrated that the disk-plus-wind model more accurately reproduced the VLTI/MIDI observations of Circinus across all wavelengths, baselines, and position angles. They concluded that the geometrically thick, warm dust structure characteristic of the traditional torus model was inconsistent with the observed data. Consequently, they proposed the disk-plus-hyperboloid wind model as a prototype for the dust structure in other AGN populations exhibiting polar dust.

In Hönig and Beckert (2011), it was proposed that polar emission could be an alternative scenario to explain the weak MIR anisotropy observed in active galaxies. This anisotropy is responsible for the strong 1:1 X-ray/MIR correlation slopes found for Type-I and Type-II AGNs. It's important to note that a toroidal clumpy distribution

also explains the weak MIR anisotropy. More sophisticated clumpy models can account for the near-infrared (NIR) excess of nuclear SEDs, either by including a polar component in addition to the torus or not (Fritz et al. (2006); Stalevski et al. (2016); Hönig and Kishimoto (2017)). These findings have significant implications for our understanding of AGNs. The discovery of a complex and dynamic dusty torus, which includes both equatorial and polar components, suggests that the interaction between the AGN and its surrounding environment is more intricate than previously thought. This complexity is evidenced by the different models that attempt to describe the torus structure, such as the clumpy torus models (Fritz et al., 2006; Stalevski et al., 2016) and the disk+wind models (Hönig & Kishimoto, 2017).

There are two different approaches to torus models: physical models and geometrical models. Physical models consider processes like blob motions along magnetic field lines, colliding magnetic clumps, radiation-pressure-supported dusty clumps, star formation-driven turbulence, supernova explosions, and AGN and stellar feedback via radiation pressure and winds, among others. They aim to answer questions about mechanisms that remove angular momentum from galactic infalling gas and mechanisms that maintain a thick gaseous structure for a long period. Hydrodynamic simulations provide a more realistic way to model this complex situation compared to analytic and semi-analytic models. Physical models are potentially more realistic, however, they are harder to compare to observations and often require extreme conditions like massive star clusters or disks, or combine multiple effects like star formation, feedback, and radiation with a high Eddington ratio to work (Netzer, 2015).

1.6 Goals and Structure of the thesis

The goal of this thesis is to study the dust structures and properties of three nearby AGNs by modelling their mid-infrared spectral energy distributions using two different models of AGN dust emission - the clumpy two-phase torus model, and the disk+cone model. The selected AGNs have been previously observed with MIR polar elongations. We compare these two models. The observations used in this thesis are discussed in Chapter 2, and the data reduction and processing are explained in Chapter 3 using Esoreflex and Python astropy library. In Chapter 4, we highlight the methods used in the thesis, explaining the SKIRT code and fitting with CIGALE. Chapter 5 contains the results and discussions.

2 Chapter 2 - Observations

2.1 Sample Selection and Instrumentation

This project focuses on three nearby active galactic nuclei (AGNs): ESO 323-G77, ESO 428-14, and NGC 5506. The observation data for these galaxies were obtained from the European Southern Observatory (ESO) archive. The data were collected using the VISIR mid-infrared imager and spectrograph mounted on the 8.2m UT3 telescope at the ESO/Paranal observatory in Chile. Additionally, ISAAC L-band data was included for ESO 323-G77. VISIR (VLT Imager and Spectrometer for mid-InfraRed) provides advanced imaging and long-slit spectroscopy capabilities in the thermal infrared range of 5 to $24\mu m$. To mitigate the high thermal background from the atmosphere and telescope, the instrument employs differential measurements using chopping (movement of the secondary mirror) and nodding (movement of the telescope itself), these were taken into account in the data reduction (Chapter 3). VISIR comprises two sub-instruments: an imager and a spectrograph, each with independent light paths, optics, and detectors. The imager features various broad and narrow band filters, along with three objectives for different spatial resolutions and fields of view. It also supports coronagraphy with an Annular Groove Phase Mask, sparse aperture masking (SAM) in both pupil and field tracking modes, and Burst Mode, which records all individual exposures of the detector rather than just the averages per nodding cycle. The spectrometer component of VISIR is divided into two arms: one equipped with a prism and low-order gratings for low and medium spectral resolution, and another with large echelle gratings for high spectral resolution. It includes multiple slits of varying widths (Lagage et al. (2004)).

The ESO ISAAC (Infrared Spectrometer and Array Camera) operates in the 1 to $5\mu m$ range and is located at the Nasmyth A focus of the VLT's UT3. It features two arms: one with a 1024 x 1024 Hawaii Rockwell array for short wavelengths (1 - $2.5\mu m$), and the other with a 1024 x 1024 InSb Aladdin array from Santa Barbara Research Center, originally for long wavelengths (3 - $5\mu m$). Since period 70 (P70), the Aladdin arm has also been used for JHK imaging (Moorwood et al. (1998)).

2.1.1 ESO 323-G77

ESO 323-G77 is a spiral galaxy located at a redshift of $z = 0.0150$, approximately $66.3Mpc$ away. It hosts an AGN classified as Seyfert 1.2, which appears to be slightly obscured (Véron-Cetty and Véron (2010)). Recent studies using X-ray observations have revealed a complex absorber and variable absorption, indicating a clumpy torus structure around the AGN (Ricci et al. (2016)).

Mid-infrared (MIR) observations have also detected polar elongation, suggesting out-

flows perpendicular to the plane of the galaxy (Asmus et al. (2016)). Photometric observations in the N-Band (8-13 μm) were recorded in 2007, 2009, 2010, 2015, and 2016, based on data obtained from the ESO Science Archive Facility (083.B-0239(A), 083.B-0239(B), 084.B-0366(E), 095.B-0376(A)).

2.1.2 ESO 428-14

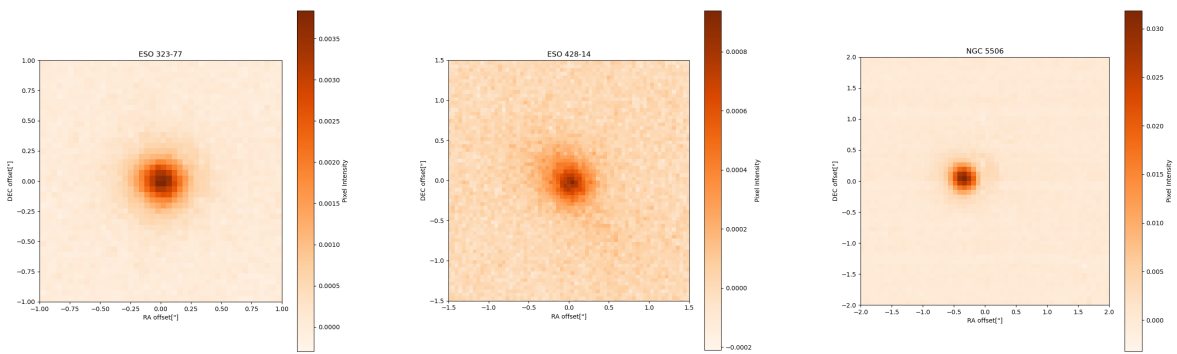
ESO 428-14 is a spiral galaxy at a redshift of $z = 0.0057$ (approximately $26Mpc$) near the Galactic plane. It hosts a Seyfert 2 (Sy 2) nucleus and features a bent jet-like radio structure aligned with a cone-like extended narrow-line region at a position angle of approximately -50 degrees (Véron-Cetty and Véron (2010); Ulvestad and Wilson (1989); Wilson and Tsvetanov (1994)).

Recent optical and near-infrared studies suggest the presence of a circumnuclear ring of star formation and a rich dust structure, contributing to its complex morphology (Ferruit et al. (2000)). Mid-infrared polar elongation has been observed, indicating active galactic outflows (Asmus et al. (2016)). Photometric observations in various N-Band filters were taken in 2007, 2018, and 2021, with spectra from 2007 and 2017, based on data obtained from the ESO Science Archive Facility (078.B-0303(A), 0100.B-0056(A)).

2.1.3 NGC 5506

NGC 5506 is a peculiar edge-on spiral galaxy at a redshift of $z = 0.0062$ (approximately $31.6Mpc$) with an AGN classified a Seyfert 1.9, a narrow-line Seyfert 1, or a Seyfert 2 nucleus. This galaxy exhibits notable properties and peculiar features. Recent X-ray observations have revealed the presence of a heavily obscured nucleus and a complex multi-phase warm absorber (Bianchi et al. (2010)). MIR observations have shown polar elongation, supporting the presence of AGN-driven outflows (Asmus et al. (2016)).

Photometric data were collected in 2005, 2006, 2010, 2018, and 2022, with spectral data from 2018 and 2022. These observations are based on data obtained from the ESO Science Archive Facility (60.A-9244(A), 076.B-0599(A), 077.B-0728(A), 084.B-0606(A), 60.A-9629(A), 099.B-0044(A)). We note that for the spectroscopic observation taken on 02-14-2022, the DIT was different, and we reject the observation for that date, this was retaken on 02-25-2025 and we got a higher flux for the spectra.



(a) ESO 323-77

(b) ESO 428-14

(c) NGC 5506

Figure 5: This figure shows the three sources after data reduction (see 3)

3 Chapter 3 - Data Reduction

The downloaded observation data of the sources, ESO 323-G77, ESO 428-14, NGC 5506, were reduced with the ESO pipeline under the user friendly environment called Esoreflex. This concentrates on high-level issues like data reduction quality and signal-to-noise (S/N) optimisation. The standard Imaging and the Spectral workflows were used for the reduction of the photometric and spectroscopic observations, respectively. With Reflex, workflow application, the data processing workflow was automated using the Kepler workflow engine. It has an advantage of having built-in tools for progress monitoring, and the ability to modify the data organisation and data flow efficiently. Figure 6 below shows the standard imaging reduction workflow used in the photometric reduction process. The Kepler workflow application provides a graphical interface to

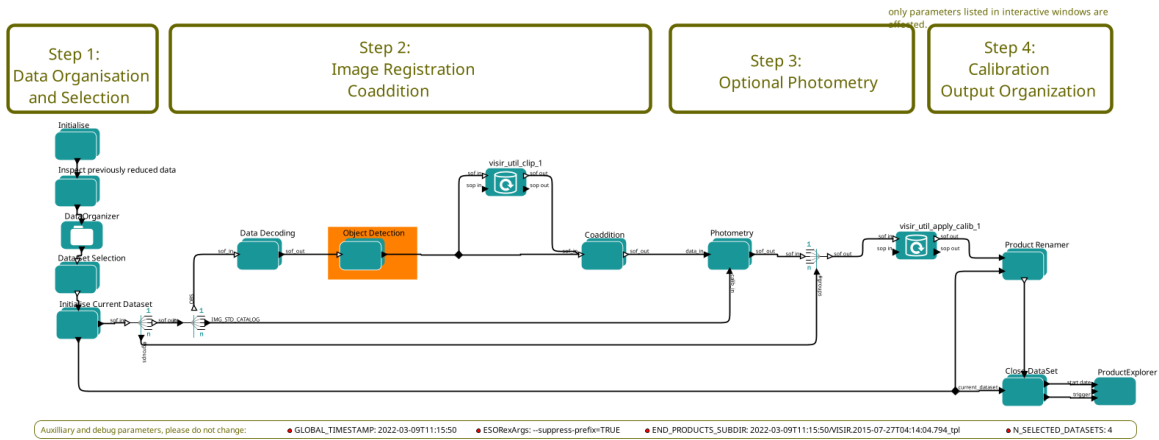


Figure 6: VISIR Imaging workflow (v. 4.4.4) (Freudling (2013))

create, edit, and execute workflows. The reflex environment consists of a number of actors that support the execution of astronomical applications. In this data reduction process explained below, the default parameters are used in the reduction except where otherwise stated.

3.1 IMAGE REDUCTION WORKFLOW

The process of image reduction begins with setting up the directory for both raw data and calibration data. The data organiser in the workflow scans the raw data directory and constructs datasets. The next step involves data selection, where datasets can be inspected and selected, and data to be included or excluded from the reduction can be specified. Following this, the data processing commences. If the data set contains calibration files, certain steps are repeated to process the calibrations.

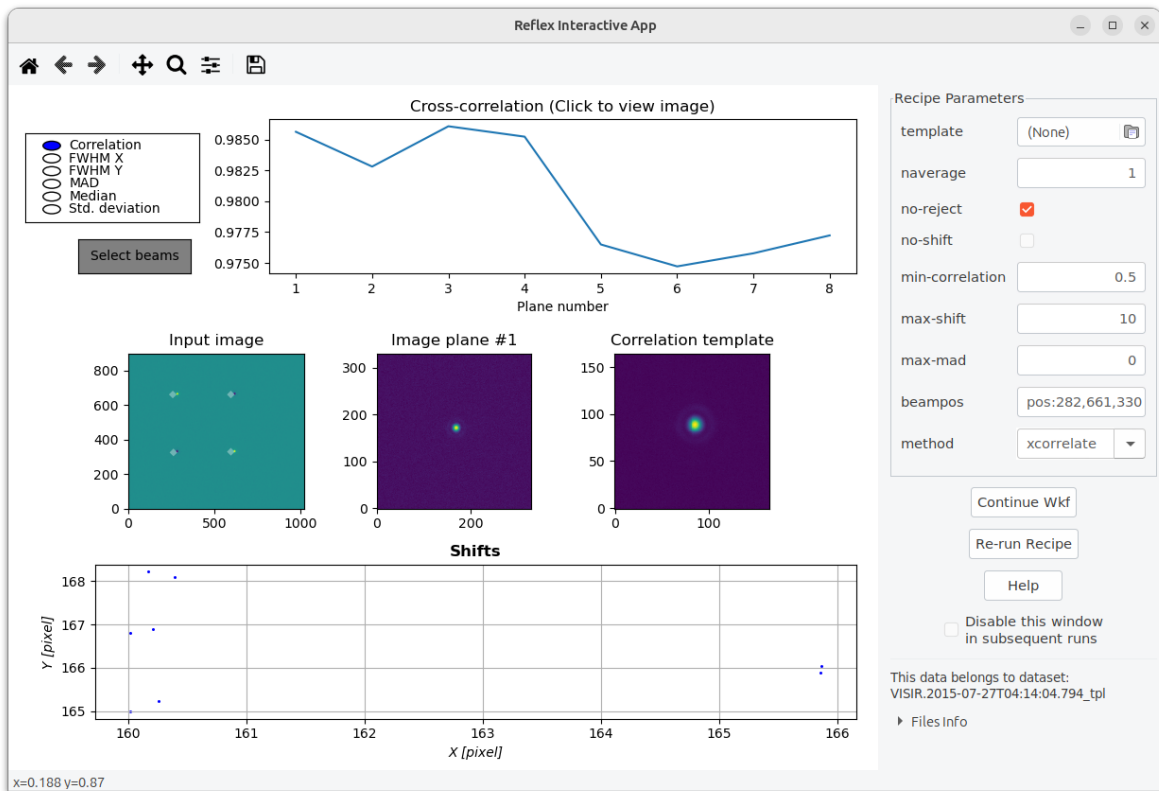


Figure 7: The interactive window for the VISIR imaging Object Detection actor.

During image processing, tasks such as bad pixel detection and cleaning, source detection, image shifts, and coaddition are performed. The recipe parameters generally remain unchanged, except in cases where frames with low cross-correlation or deviation need to be rejected to enhance the overall quality of the reduction. With the no-reject parameter, we choose if true images with bad statistics would be accepted and if no shift correction is done. With min-correlation parameter, we determine the minimal correlation to the template to be accepted, with max-shift, we select the maximal allowed shift from the template for an object to be accepted, and max-mad represents the median absolute deviation for an object to be accepted. Additionally, some frames are averaged with the naverage parameter, to improve the signal-to-noise ratio. Optionally, photometry and flux calibration are conducted if standard flux is available. In the reflex interactive app, we also select a method for the determination of beam shifts, either by the brightest pixel which is default, or by the cross correlation shifts. The photometry is carried out using the Python Astropy library.

3.2 SPECTROSCOPY WORKFLOW

The process also begins with the input of the directory of the raw spectra datasets, which includes the raw and processed calibration files. Using the aperture editor GUI, an aperture definitions file is created and passed to the `visir old spc obs recipe`. In figure 8, optimal spectral extraction is illustrated, showing the combined 2D spectrum, aperture width, and some parameters including `destripe_iterations`, kept at 15, `destrip_morpho` and `fixcombi` for distortion correction in combined image, left unchecked. Other parameters are; the detector gain at 0.75, `ox_kernel = 3` for size of square smoothing kernel before optimal extraction with median filter used, `ox_niters = 2` representing the number of optimal extraction iterations to perform, `ox_sigma=5`, the sigma used for clipping in the optimal extraction. The width of the smoothing window is adjusted with `ox_smooth` parameter. With each resulting pixel being an average of corresponding pixel value in interpolated image, the parameter `rej` determines if the smallest and the largest pixels are to be ignored in the averaging. The read-out noise could be specified with the parameter `ro_noise`(left at 14.5). Slit skew, spectrum skew, and detector vertical curvature parameters are adjusted with `slit_skew`, `spectrum_skew`, and `vert_arc` respectively.

3.3 Python Script

For the processing of reduced data, a Python script (Appendix A) was written. It begins with the import of FITS files, the photometry of the openings and the construction of the SED. The script uses `astropy`, `photutils`, and `scipy` libraries to handle astronomical data, perform statistical analyses, and generate visuals, among other things. The code begins with the import of Python libraries needed to perform numerical operations such as `numpy`, `astropy`, `model tasks`, and `photometric calculations`. A global dictionary `params` is defined to adjust the appearance of the tables, ensuring that labels and titles are displayed in the appropriate size and format. The script then defines a set of global patterns to locate the relevant FITS files containing spectroscopic and photometric data. These files correspond to observations of the AGN, and related standard stars. In Appendix B, the results from the photometry and gaussian fitting is shown. The spectroscopic files are read in for processing and SED construction. The calibrated intensity and wavelength data are obtained from the file. the intensity data is converted to flux, removing NaN values and applying edge correction. The resulting data is then cleaned of outliers using the `remove spikes` and `sigma clip` functions. The wavelength and flux data are stored for subsequent plotting.

The processed spectroscopic data are plotted to produce a Spectral Energy Dis-

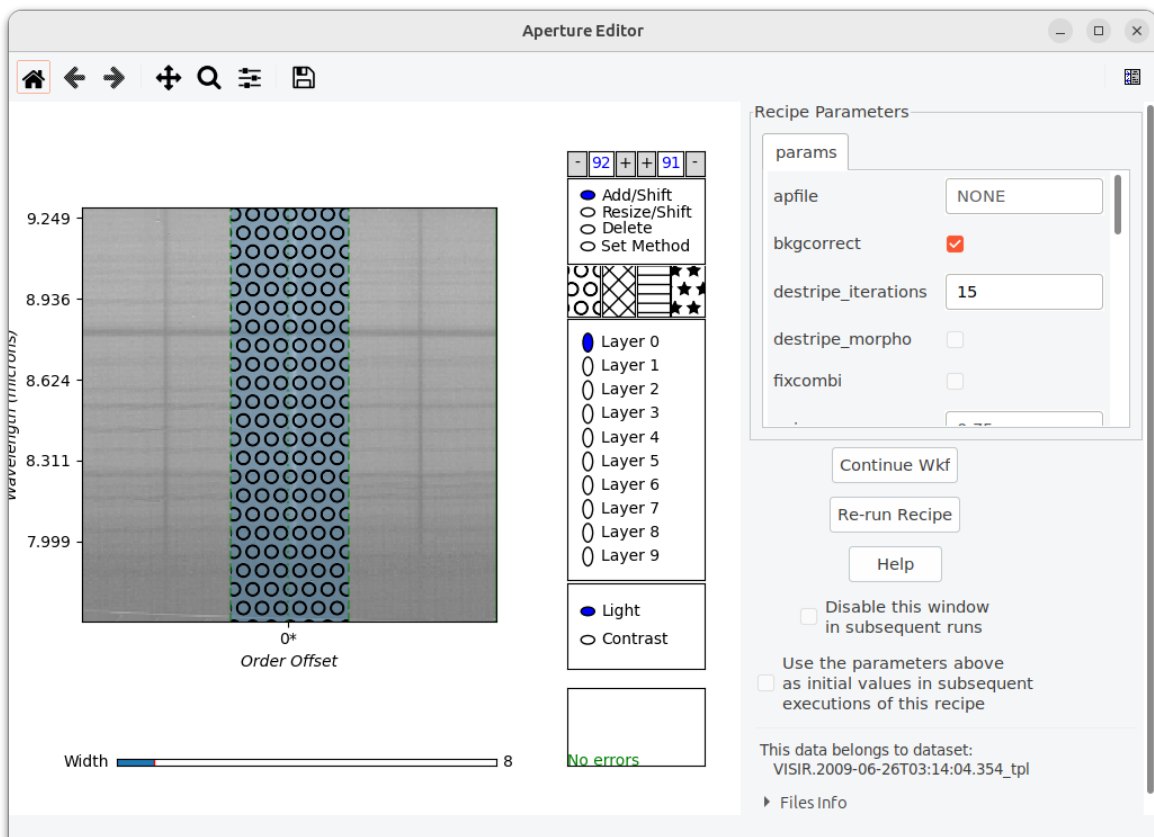


Figure 8: Long slit mode: optimal extraction aperture being configured.

tribution (SED). The subsequent step involves binning the flux data to enhance the clarity of the spectrum by averaging adjacent spectral points. It is adequate for the bin sizes to be at least a few times the spectral resolution, $\delta\lambda$, where $\delta\lambda = 0.0028\mu m$ at $10\mu m$, with a resolving power of $R = 350$. Therefore, the spectra can be divided into several points, each with a width of no less than twice the spectral resolution. For the spectrum of NGC 5506, we opted to divide it into 9 bins to effectively capture the silicate absorption feature. The spectra of ESO 323 and ESO 428 were binned into 6 points.

Error bars are included in the plot to represent the statistical uncertainties associated with the measurements. Next, aperture photometry is performed centred on the brightest pixel in the image. The background flux from an annulus is calculated and subtracted to give the total photometric flux of the galaxy.

Standard stars are fit using a combination of an Airy disk model and a constant background. These fits are later used as initial guesses for fitting Gaussian models to the images of observations. The script employs both single- and double-Gaussian models to account for the flux contributions from the active galactic nucleus (AGN) and the unresolved components. To determine the best fit between the single and double Gaussian models, the script calculates the reduced chi-squared statistic and the Bayesian Information Criterion (BIC) for each model. The model with the lower BIC is selected as the best fit. The AGN contribution to the flux is then extracted from the best fit model.

4 Chapter 4 - Methods

Studies of dust in AGN studies and simulates the properties of dust surrounding a black-hole. It involves the study of dust composition and distribution, interaction with light and its effect on the SED, and impacts on observation like extinction, reddening, and infrared emission. This is very important in understanding the structure and unification of AGNs, constraining AGN properties, and feedback mechanisms and galaxy evolution studies.

Radiative transfer (RT) simulations give a detailed understanding of how light from the black-hole and accretion disk interact with surrounding gas and dust, and how energy is being absorbed, and re-emitted at different wavelengths. They also help in the correction of extinction and reddening caused by dust, thus allowing more accurate determination of intrinsic AGN properties. With RT simulations, we can constrain AGN properties, test and refine theoretical models, and study of AGN at different parts of the electromagnetic spectrum.

In this chapter, we describe the method used to model dust in AGN using Monte Carlo radiative transfer simulation with the SKIRT code and fitting with the CIGALE code. The reason for this is to investigate and compare two dust models, the skirtor model, and the disk+cone model.

4.1 Monte Carlo Radiative Transfer

The Monte Carlo Radiative Transfer (MCRT) method is a computational technique used to simulate the transfer of radiation through a medium, for example, gas and dust around a black-hole. Instead of directly solving the radiative transfer equation, MCRT simulates the process by following the paths of a large number of photon packages as they interact with the medium. These photon packages are like little bundles of light that travel through the dust, and their interactions (absorption, scattering, and re-emission) are determined randomly based on probabilities derived from the dust properties and the radiation field itself. At the end of the simulation, the behaviour of all the photon packages is analysed statistically to figure out the overall radiation field, allowing the creation of synthetic images and spectra that can be compared to real observations.

Cashwell and Everett (1959); Witt (1977) described in detail the path of a single 'photon package' through the MCRT calculation. This begins with the emission of a single photon from a luminous source, a star or an AGN. The photon then travels through the dust cloud, and its interactions with dust grains—both scattering and absorption—are simulated based on the properties of the dust and the wavelength of

the photon. When a photon is absorbed, it deposits its energy into the dust grain, causing the grain to heat up. This absorbed energy is later re-emitted by the dust, primarily at infrared wavelengths. The re-emitted photon then begins its own journey, and this cycle of scattering, absorption, and re-emission continues until the photon either escapes the dust cloud or is absorbed without further re-emission.

An accurate representation of the dust properties is essential for a realistic MCRT simulation. Dust albedo, scattering phase function, and extinction and absorption coefficients all play critical roles in determining how photons interact with dust grains. It is emphasized that dust scattering is usually anisotropic, so the direction of scattering is not completely random, but it is influenced by the initial direction and properties of the dust grains.

4.2 SKIRT Code

The SKIRT¹ code is a three-dimensional radiative transfer tool designed for the simulation of complex interactions between radiation and matter in astrophysics.

At its core, SKIRT uses the MCRT method to simulate the propagation of light through a dusty medium like the surrounding of a black hole, galaxies, circumstellar disks and star-forming regions. As previously mentioned, the MCRT simulations follow the path of countless individual photons in a grid as they interact with dust grains through scattering, absorption, and re-emission events. This probabilistic approach allows for the accurate modelling of complex, three-dimensional dust distributions and the resulting radiation fields.

Initially developed to investigate the effects of dust absorption and scattering on the observed kinematics of dusty galaxies, the Monte Carlo method has since been adapted to self-consistently calculate the dust emission spectrum under the assumption of Local Thermodynamic Equilibrium (LTE). SKIRT has been widely applied to model the dust emission in various astrophysical environments, including galaxies and circumstellar disks.

In recent years, SKIRT has also been utilized for the detailed modelling of dusty tori in AGN, enabling the study of complex radiative processes within these structures. By simulating the interaction of radiation with dust grains, SKIRT provides insights into the geometry, composition, and temperature distribution within AGN tori, contributing to our understanding of their role in the obscuration and re-emission of radiation from the central engine.

Some of the key features of SKIRT include the ability to model any one-, two-, or three-dimensional geometry, a library of built-in geometries, radiation sources,

¹skirt.ugent.be

and dust properties, and the ability to import models from hydrodynamic simulations. Additionally, SKIRT can include instruments for recording "observed" spectra, images, and data cubes.

SKIRT has been used in many studies, including those on the dust energy balance in galaxies (De Looze et al. (2010); Baes et al. (2010)), investigations of the structure and observable properties of AGN dusty tori (Stalevski et al. (2012a,b), and studies of the effects of different parameters—such as torus opening angle and dust optical depth—on the observed SED of AGNs (Yang et al. (2020)).

Overall, SKIRT is a powerful and versatile code that is well-suited for studying radiation transfer in astrophysical environments.

4.3 MODELS

The two models used in this study are the Torus model from Stalevski et al. (2016) (SKIRTOR²) and the disk+cone model based on Stalevski et al. (2017, 2019); Stalevski et al. (2023).

4.3.1 SKIRTOR

Unlike the Fritz et al. (2006) model that describes the torus as a smooth, dusty structure with a range of geometries and dust compositions, dust in the Skirtor model is distributed in a two-phase medium - high-density clumps embedded in a smooth lower density dust component. The dust composition is 53% silicate grains and 47% graphites. Studies using hydrodynamical simulations and taking into account other processes such as self-gravity of the gas, radiative cooling and heating due to supernovae or accretion disk, found that the interstellar medium around the AGN would result in a multiphase filamentary structure and this has been observed in central regions of Milky Way (the so-called Central Molecular Zone and Circumnuclear Disk) and it has been suggested that they represent a remnant of a dusty torus that may have played a role in past AGN phases of our Galaxy.

This composite model is more realistic because the volume between the clumps is filled with dilute dusty gas, which absorbs part of the optical-UV radiation and part of the locally emitted NIR and MIR radiation. The clumpy nature of the torus has significant implications for the infrared emission, as it allows for more complex and realistic modeling of the radiative transfer processes within the torus. This model can better reproduce the observed infrared spectra of AGNs, considering the variability and anisotropy in dust distribution.

²<https://sites.google.com/site/skirtorus/>

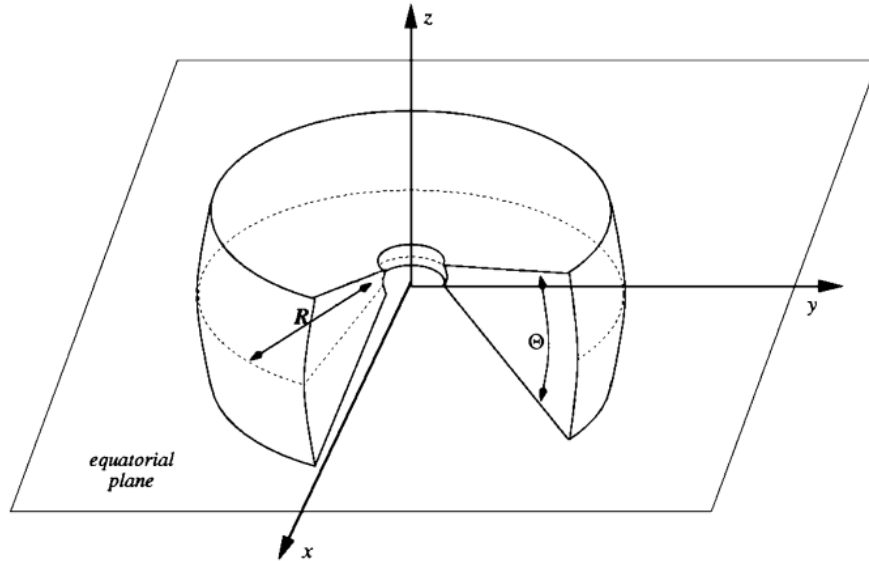


Figure 9: Schematics for the torus model.

This study presents an analysis of the mid-infrared (MIR) spectral energy distributions (SEDs) of three local active galactic nuclei (AGNs) exhibiting polarized dust emission. Two dust emission models were employed: the Skirtor16 model (Stalevski et al., 2016) and a novel disk-plus-cone model (Stalevski, 2017, 2019, 2023). While the more sophisticated disk-plus-hyperboloid model is generally more accurate, the limited spatial resolution of our VISIR observations necessitated the use of the disk-plus-cone model for this investigation. A. Božilović developed the SED model library for this research as part of their Master of Science thesis. This new disk+cone model has parameters such as the average disk edge-on optical depth at $9.7\mu m$, the power-law exponent that sets the radial gradient of the dust density, the power-law exponent that sets the dust density with polar angle, the disk opening angle (the angle measured between the equatorial plane and the edge of the ‘torus’), the ratio of the outer radius to the inner radius (set to 5), the conical shell average edge-on optical depth at $9.7\mu m$, the conical shell power-law exponent that sets the radial gradient of dust, the conical shell angle measured between the equatorial plane and the edge of the torus, the conical shell ratio of outer to inner radius (with possible values of 50, 100, and 200), and the tilt and inclination of the accretion disk.

Table 1: Model parameters for the clumpy two-phase torus model, Skirtor.

Parameters	Description	Possible values
R_0/R_d	Ratio between the outer and inner radius of the torus.	10, 20, 30
$\sigma[^\circ]$	Half opening angle of the torus.	10, 20, 30, 40, 50, 60, 70, 80
p	Power-law exponent that sets radial gradient of dust density.	0.0, 0.5, 1.0, 1.5
q	Power-law exponent that sets polar gradient of dust density.	0.0, 0.5, 1.0, 1.5
$\tau_{9.7\mu m}$	The $9.7\mu m$ average edge-on optical depth.	3, 5, 7, 9, 11

4.4 CIGALE

The Code Investigating GALaxy Emission (CIGALE³) is a comprehensive tool designed to efficiently model the spectral energy distributions (SEDs) of galaxies across a broad range of wavelengths, from radio to X-ray (Boquien et al. (2019)). By analyzing the SEDs, CIGALE enables the extraction of crucial information regarding the physical properties of galaxies. One of CIGALE’s most significant strengths lies in its modular architecture, which facilitates the modification and extension of its capabilities, allowing for tailored modelling depending on the specific research requirements.

Star Formation History (SFH): The SFH module allows users to specify how the rate of star formation in a galaxy has evolved over time. CIGALE offers several SFH modules, including the `sfh2exp` module, which models the SFH using one or two decaying exponentials. Other available SFH modules include those for delayed and periodic star formation histories. In this study, the `sfh2exp` module was utilized due to its suitability for our research objectives.

Nebular Emission: This module accounts for the emissions originating from star-forming regions ionized by hot, young stars. However, for the purposes of this project, the nebular emission module was excluded, as our sources do not exhibit star formation activity. **Stellar Populations:** CIGALE incorporates two stellar population modules, which are based on the single stellar population (SSP) libraries developed by Bruzual & Charlot (2003) and Maraston (2005). These are referred to as the `bc03` and `m2005` modules, respectively (Bruzual and Charlot (2003); Maraston (2005)).

³<https://cigale.lam.fr/>

Table 2: Parameters for the disk+cone model.

Parameters	Description	Possible values
DSK.t	Average edge-on optical depth at 9.7 micron of disk.	2, 4, 6, 8, 10
DSK.p	Power-law exponent that sets radial gradient of dust density.	0.0, 1.0
DSK.q	Power-law exponent that sets polar gradient of dust density	0.0, 1.0
DSK.oa [°]	Half-opening angle of the dust-free (or polar-dust) cone.	10, 20, 30, 40
DSK.R	Ratio of inner radius to outer radius.	5
CON.t	Average edge-on optical depth at 9.7 micron of the conical shell.	-1.0, -0.1, 10.0
CON.p	Conical shell power-law exponent that sets radial gradient of dust density.	0.0, 0.1
CON.oa[°]	Conical shell angle measured between the equatorial plane and edge of the torus.	20, 30, 40
CON.R	Conical shell ratio of outer to inner radius.	50, 100, 200
AD.tl[°]	Tilt of the accretion disk.	0, 30, 45
AD.i[°]	Inclination, i.e. viewing angle, position of the instrument w.r.t. the AGN axis.	0, 10, 20, 30, 40, 50, 60, 70, 80, 90

Dust Attenuation: This module simulates the absorption and scattering of light by dust within the interstellar medium (ISM) of a galaxy, particularly at shorter wavelengths. Various attenuation curves, such as the Calzetti law, can be applied to model these effects (Calzetti et al. (2000)).

Dust Emission: The dust emission modules in CIGALE are designed to simulate the re-emission of absorbed energy by dust at longer, infrared wavelengths. These simulations utilize models such as those from Dale et al. (2014) and Draine and Li (2007).

AGN Emission: CIGALE also includes modules to model the contributions of active galactic nuclei (AGN) to the overall SED. These modules account for different AGN components, including the accretion disk, dusty torus, and polar dust. The Fritz smooth torus model and the SKIRTOR 2016 clumpy two-phase torus model were incorporated into the AGN modules used in this study (Fritz et al. (2006); Stalevski et al. (2016)). Additionally, a model SED library for the disk+cone model, developed by A. Božilović (Božilović (2019)) in their M.Sc. thesis based on disk+cone model in Stalevski et al. (2017, 2019), was integrated into CIGALE to enhance the AGN modeling capabilities. This model is similar to model described in Hönig (2019).

5 Chapter 5 - Results and Discussions

In this chapter, we present the results and conclusions of the project. We include plots of both the spectroscopic and photometric data, along with the SED fitting results for both the torus model and the disk+cone model. Additionally, we provide probability density plots for the various parameters used in the fitting process.

Table 3: Chi-square of the Fitting with the Skirtor and the Disk+cone model.

AGN	Model	χ^2
ESO 323-77	Skirtor	1.3
	Disk+cone	0.61
ESO 428-14	Skirtor	0.49
	Disk+cone	4.7
NGC 5506	Skirtor	0.039
	Disk+cone	4.1

The AGN photometry flux is obtained from the gaussian fitting. It is not unexpected that the points are lower than that seen from the aperture photometry because the flux from the aperture photometry may include some host galaxy contribution. When we compared the data with MIRI, we find that it matches well. It is to be noted that the full aperture photometric points were used for the fitting with CIGALE because the emission is AGN dominated and the flux from the gaussian fit might have missed out some contribution in the polar region.

In the SED plots in Figures 10, 11, 12, the yellow dots are the spectro-photometric points from the binned spectra, the black dots represent the flux acquired from aperture photometry, and the red dot represents the AGN flux from the Gaussian fitting. The y-axes of the probability density function (PDF) plots show how likely certain values of the fitting parameters on the x-axes are. In other words, they represent the likelihood of different parameter values, with higher points on the y-axes indicating more likely values. This probability density helps us see which parameter values fit the data best.

5.1 ESO 323-77

Figures 13, 14, 15, 16 show the results of the fitting SED fitting of ESO 323-77 with both the SKIRTOR and the disk+cone model. Figures 14 and 16 show the probability

5.2 ESO 428-14

Figures 17, 18, 19 20 show the results of the fitting SED fitting of ESO 323-77 with both the SKIRTOR and the disk+cone model. Figures 18 and 20 show the probability density plots of the fitting parameters. From top-left in figure 18, the parameters are; the $9.7\mu m$ average edge-on optical depth, the ratio between the outer and inner radius of the torus, the torus opening angle, power-law exponent that sets polar gradient of dust density, the AGN inclination, and the power-law exponent that sets the radial gradient of the dust density.

The PDF plot indicates that the model prefers higher optical depth values, bigger inclination and opening angle. This is expected because ESO 428 is a Type-2 AGN.

In figure 20, the first row from left to right shows the PDF plots for the parameters; the $9.7\mu m$ average edge-on optical depth of the disk, the conical shell ratio of the outer to inner radius, and the conical shell angle measured between the equatorial plane and the edge of the torus. In the second row, the PDF plots from left to right are for the parameters; the dust density gradient with polar angle, the conical shell power law exponent that sets the gradient of the dust density, the inclination, and the tilt of the accretion disk.

We note here also that the model preferred low values of the disk optical depth, smaller cone opening angles, but higher inclination.

5.3 NGC 5506

Figures 21, 22, 23, 24 show the results of the fitting SED fitting of ESO 323-77 with both the SKIRTOR and the disk+cone model. Figures 22 and 24 show the probability density plots of the fitting parameters. In figure 22, from top-left, the parameters are; the $9.7\mu m$ average edge-on optical depth, the ratio between the outer and inner radius of the torus, the torus opening angle, power-law exponent that sets polar gradient of dust density, the AGN inclination, and the power-law exponent that sets the radial gradient of the dust density.

The model shows a spread in the values for the optical depth, preferring moderate values, bigger angles are preferred for the inclination, and moderate values for the opening angle. In figure 24, The first row from left to right shows the PDF plots for the parameters; the $9.7\mu m$ average edge-on optical depth of the disk, the conical shell ratio of the outer to inner radius, and the conical shell angle measured between the equatorial plane and the edge of the torus. In the second row, the PDF plots from left to right are for the parameters; the dust density gradient with polar angle, the conical shell power law exponent that sets the gradient of the dust density, the inclination, and

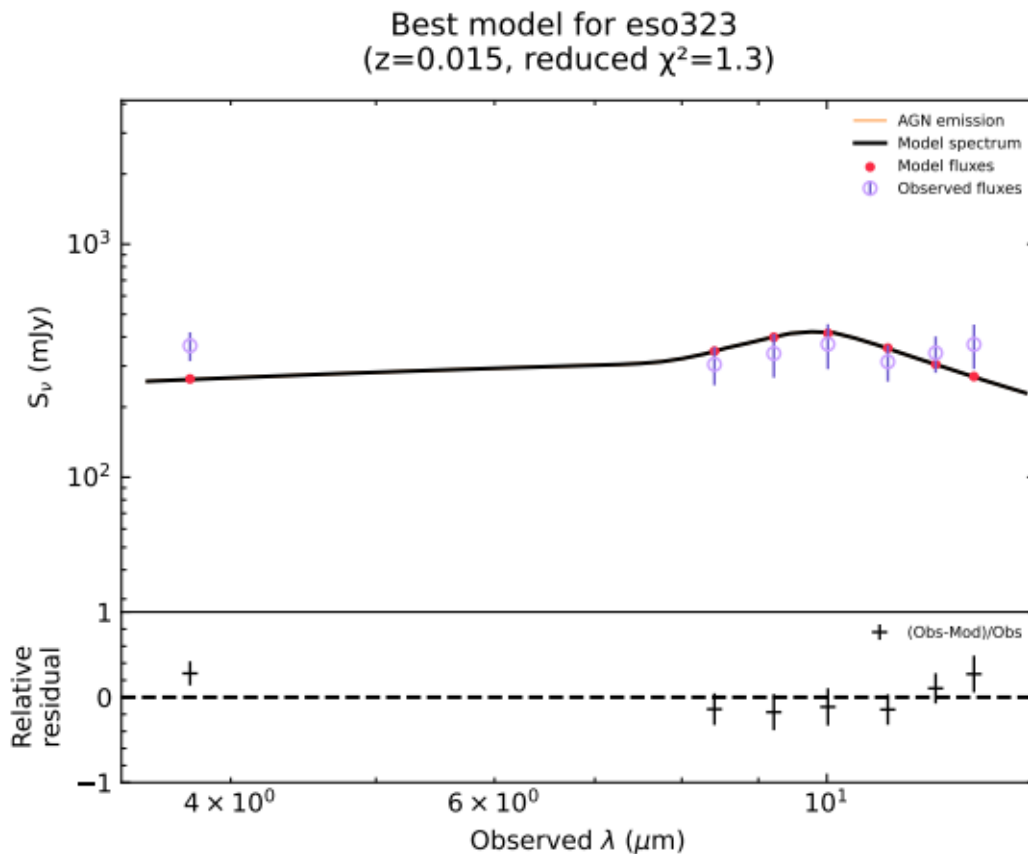


Figure 13: This plot shows the fitting of the ESO 323-77 SED with the Skirtor model.

the tilt of the accretion disk. We note that the model preferred lower values of the disk optical depth, larger cone opening angles within the range, but moderate inclinations. This best fit model is very close to being a Type-1 AGN.

For ESO 323-77, where the mid-infrared SED is mostly flat, we see that both the SKIRTOR and the disk+cone models fit the SED well, with the disk+cone model performing slightly better. However, for NGC 5506 and ESO 428-14, which have a deep silicate feature at 9.7 microns, we see a better fit of the SED with the SKIRTOR model. From the residual plot, we observe that the silicate absorption feature is not well fitted. The fit could be improved by accounting for infrared extinction due to foreground absorption by the host galaxy, as well as by the interstellar and intergalactic medium. However, CIGALE does not offer this functionality. We conclude that the parameter value ranges of the disk+cone model should be expanded to incorporate dust extinction and the silicate absorption feature.

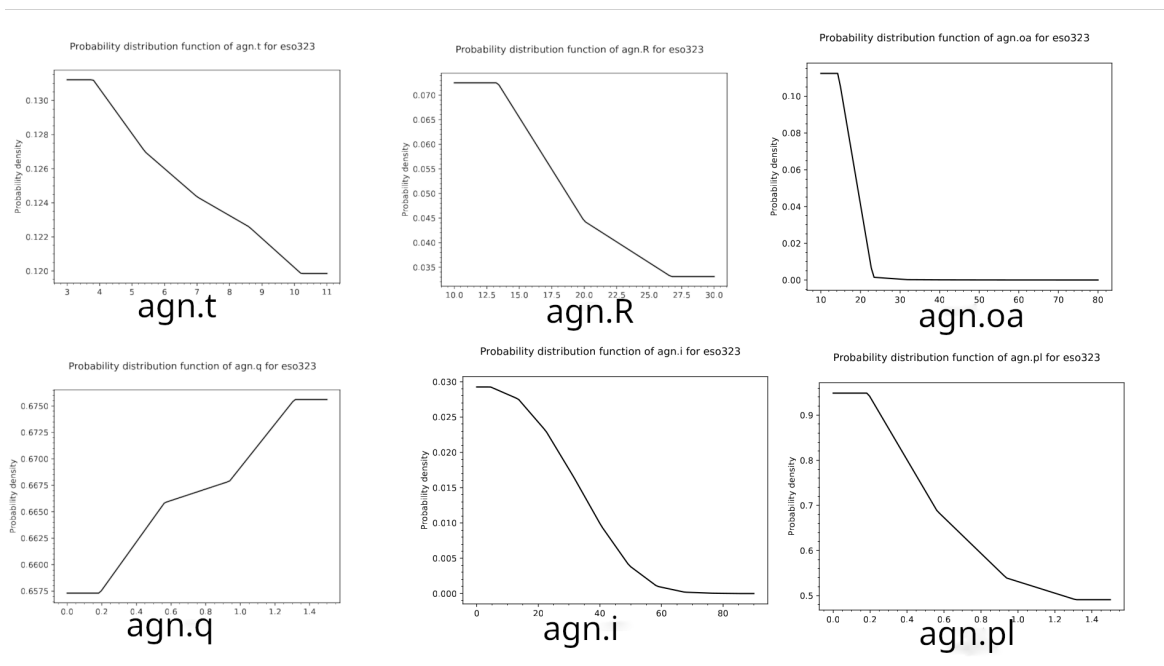


Figure 14: Probability density function plots of parameters with SKIRTOR model for ESO 323-77.

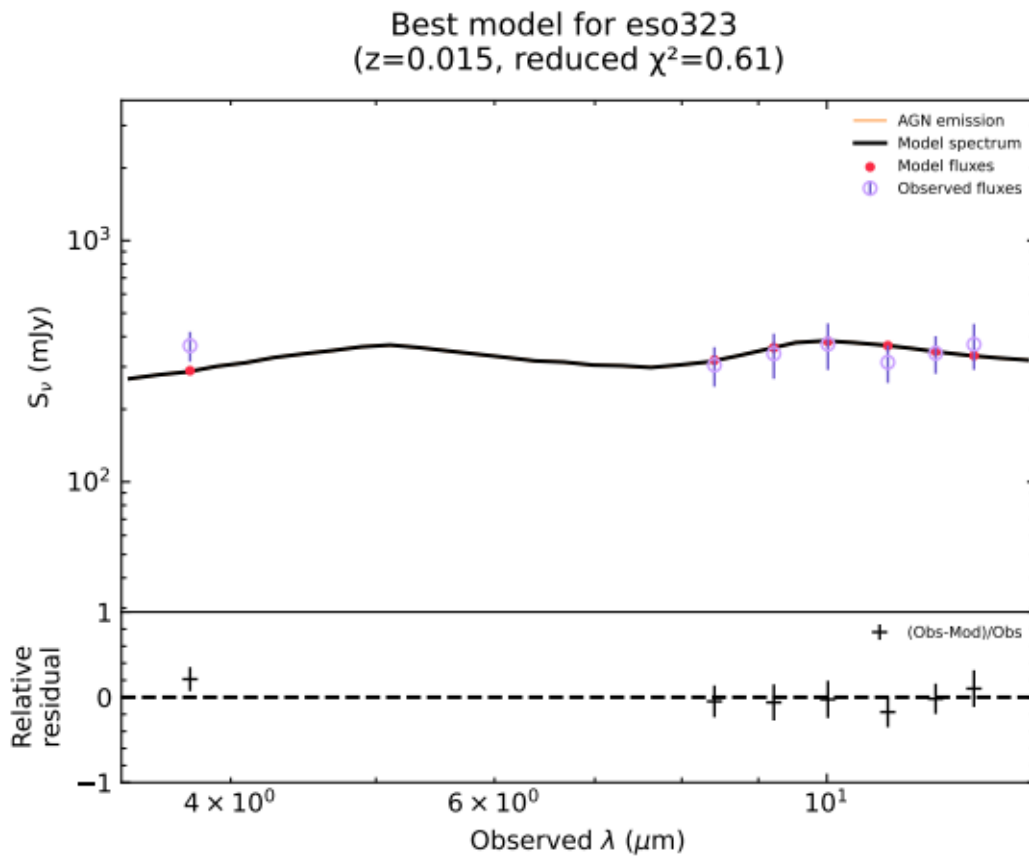


Figure 15: This plot shows the fitting of the ESO 323-77 SED with the Disk+cone model.

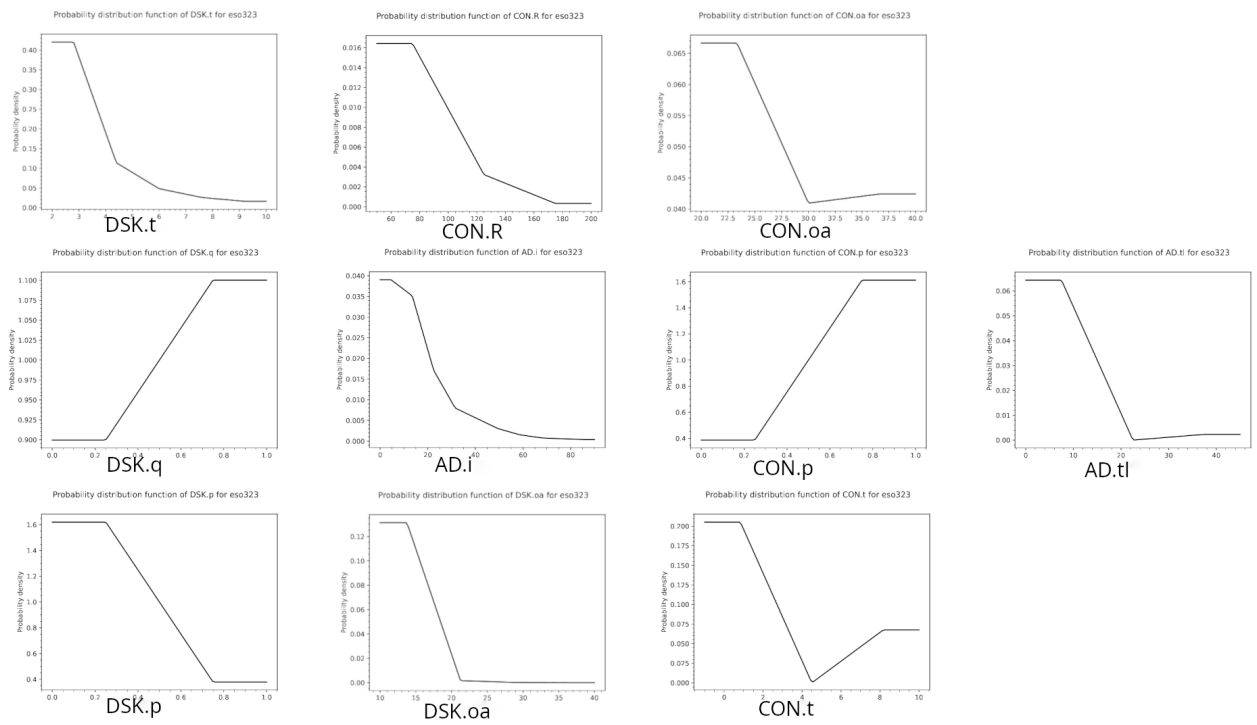


Figure 16: Probability density function plots of parameters with the Disk+cone model for ESO 323-77.

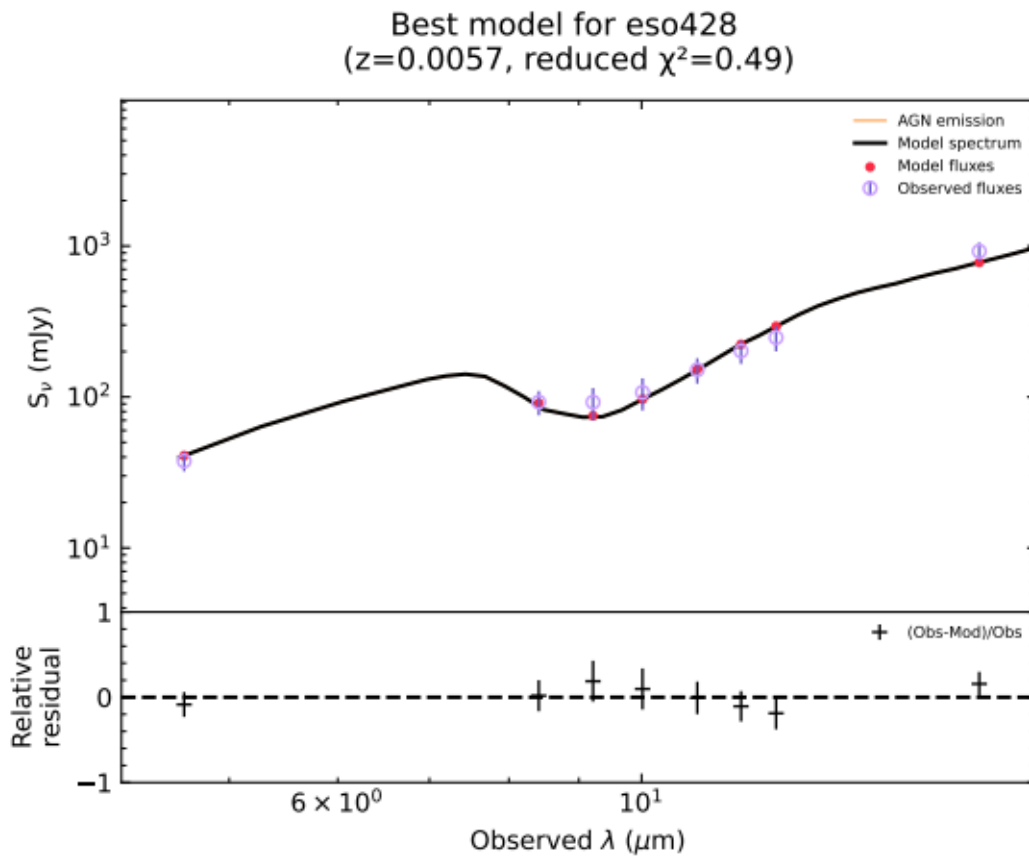


Figure 17: This plot shows the fitting of the ESO 428-14 SED with the SKIRTOR model.

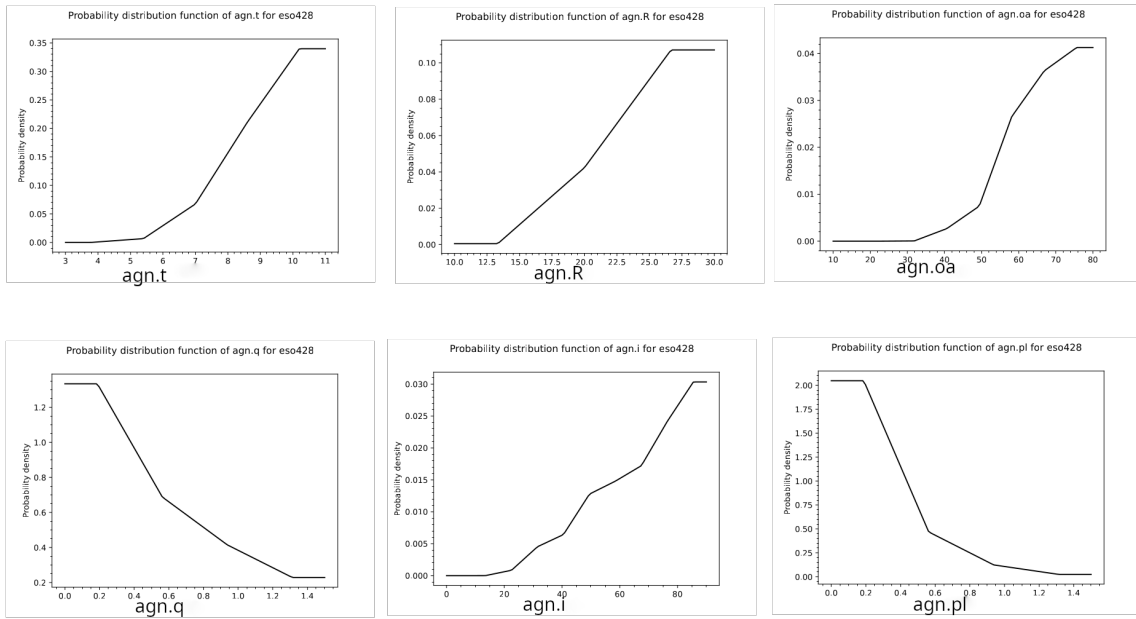


Figure 18: Probability density function plots of parameters with Skirtor model for ESO 428-14.

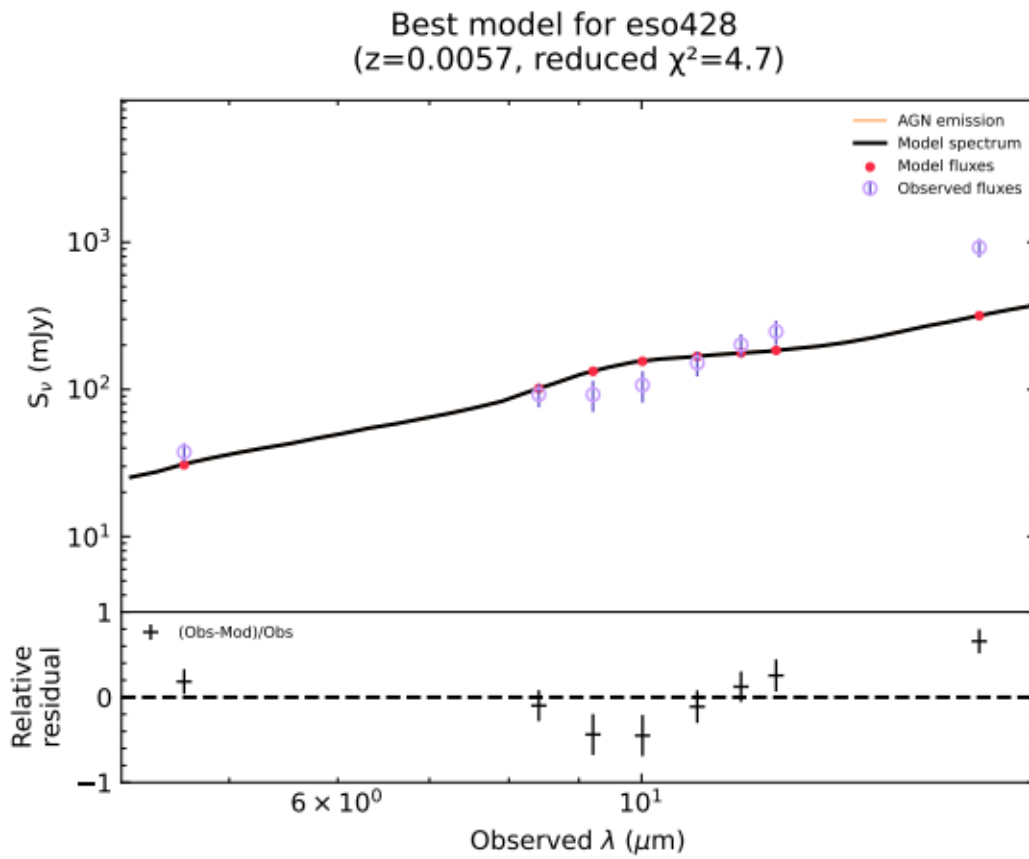


Figure 19: This plot shows the fitting of the ESO 428-14 SED with the Disk+cone model.

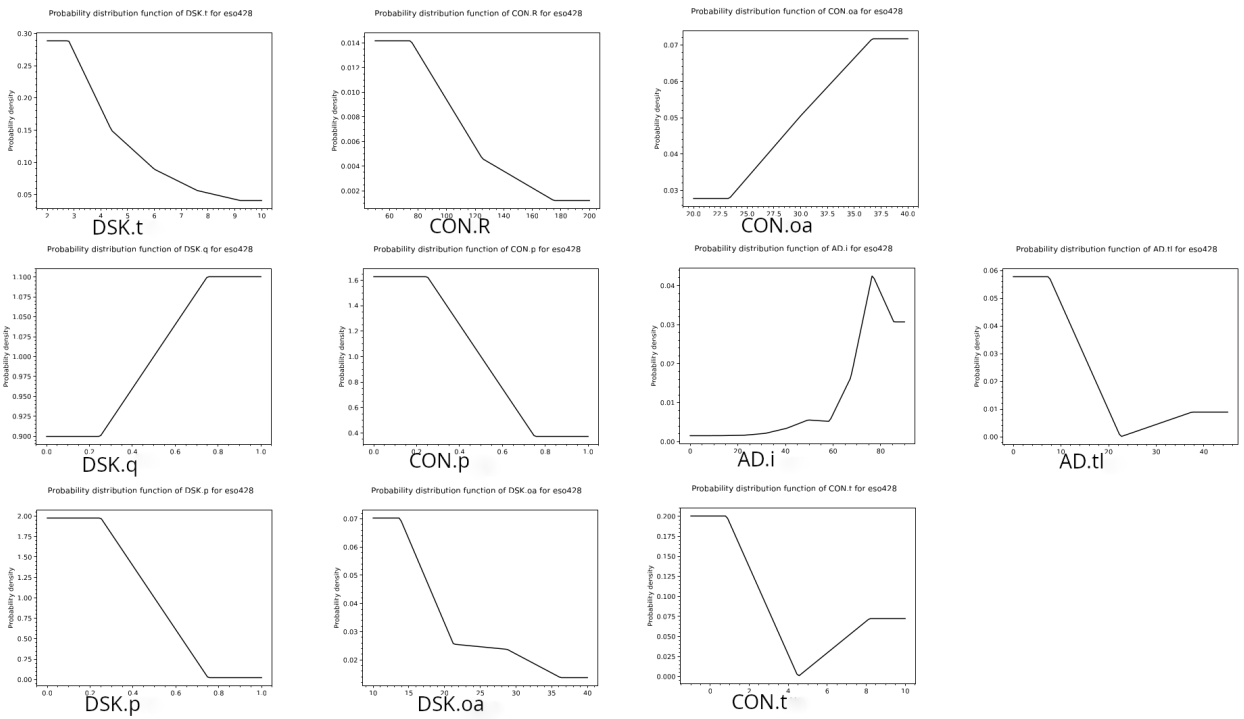


Figure 20: Probability density function plots of parameters with the Disk+cone model for ESO 428-14.

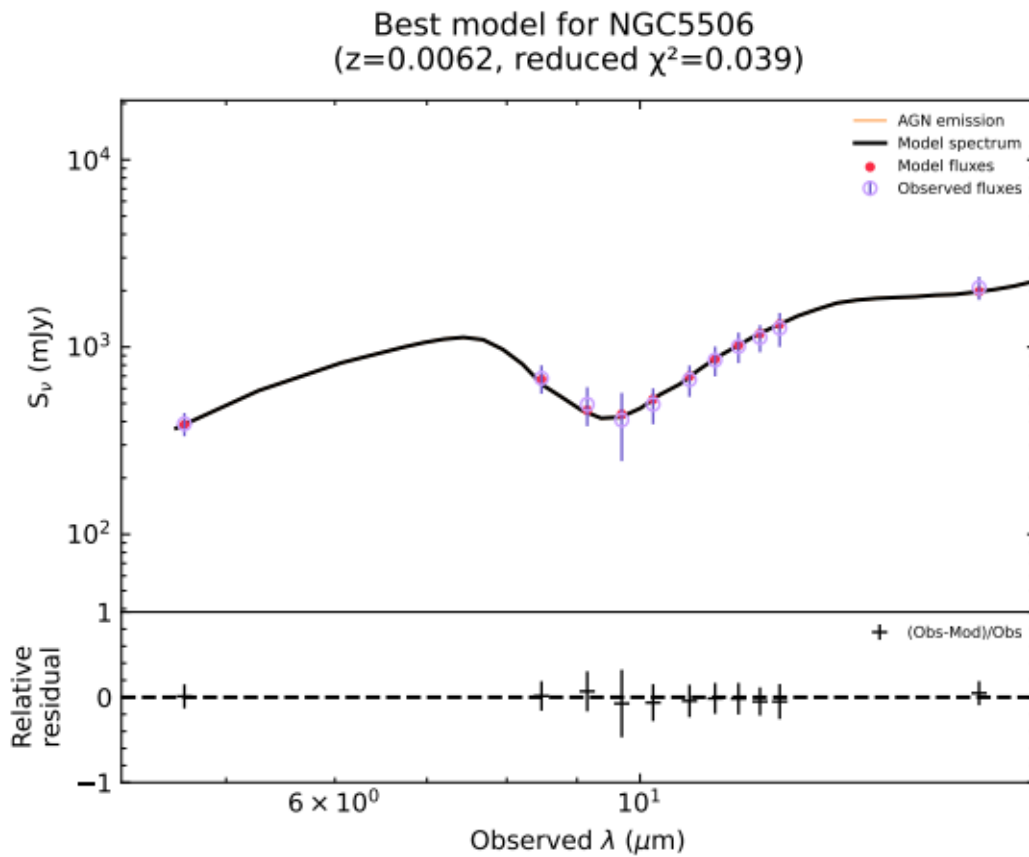


Figure 21: This plot shows the fitting of the NGC 5506 SED with the SKIRTOR model.

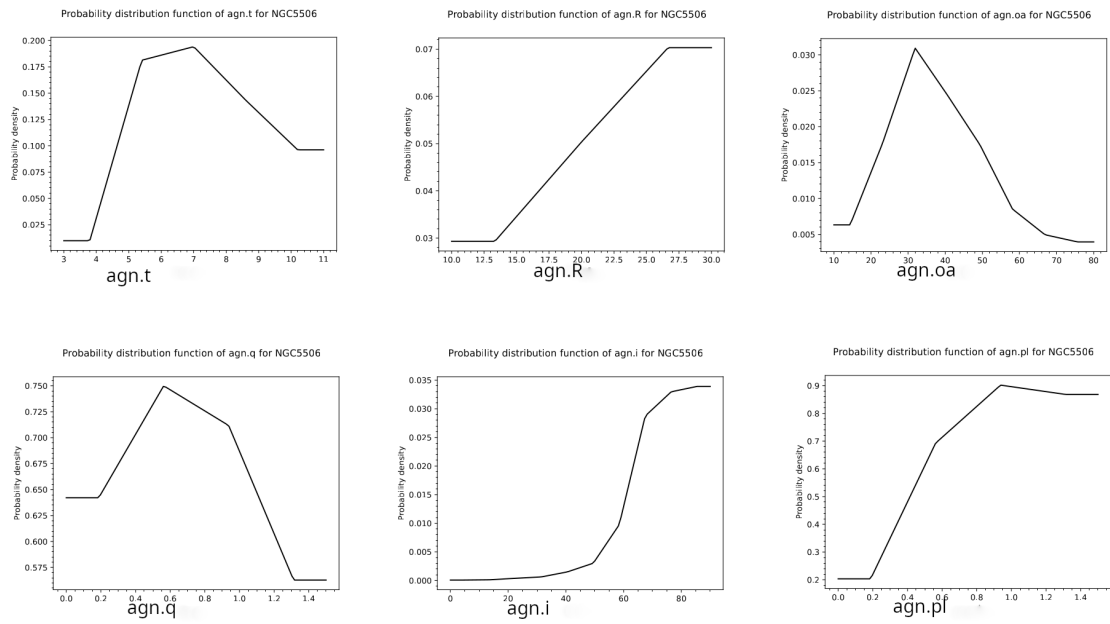


Figure 22: Probability density function plots of parameters with Skirtor model for NGC 5506.

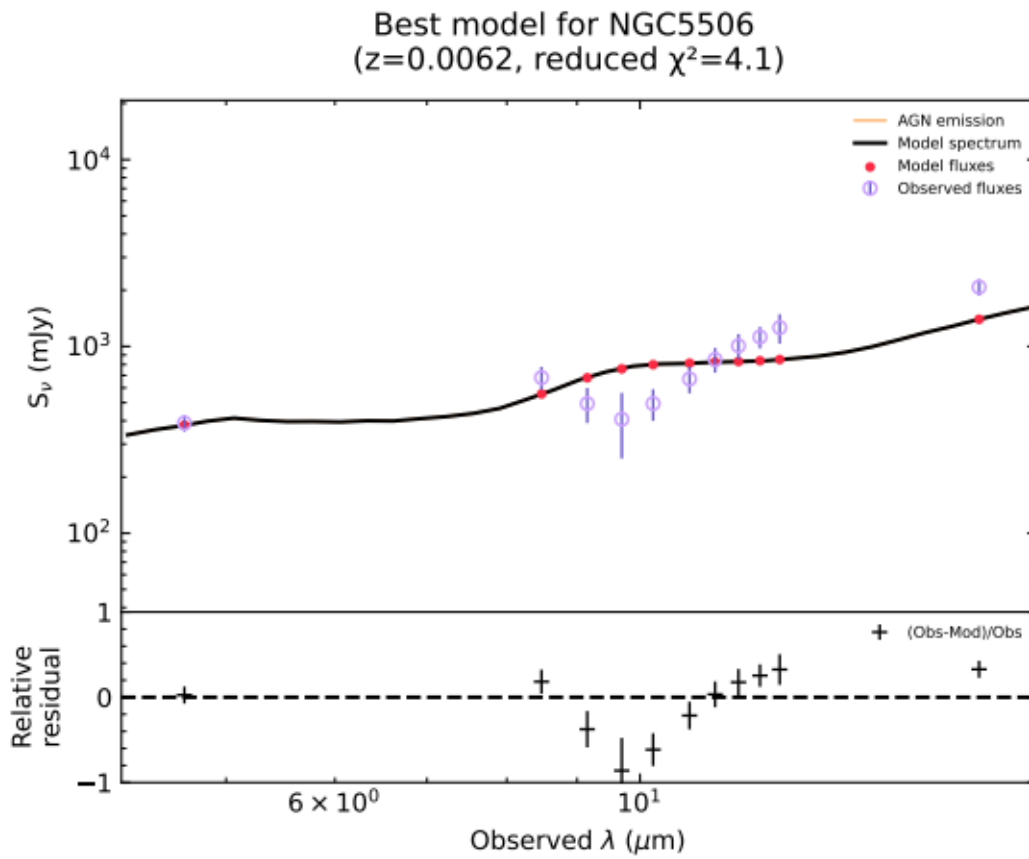


Figure 23: Disk+cone model for NGC 5506

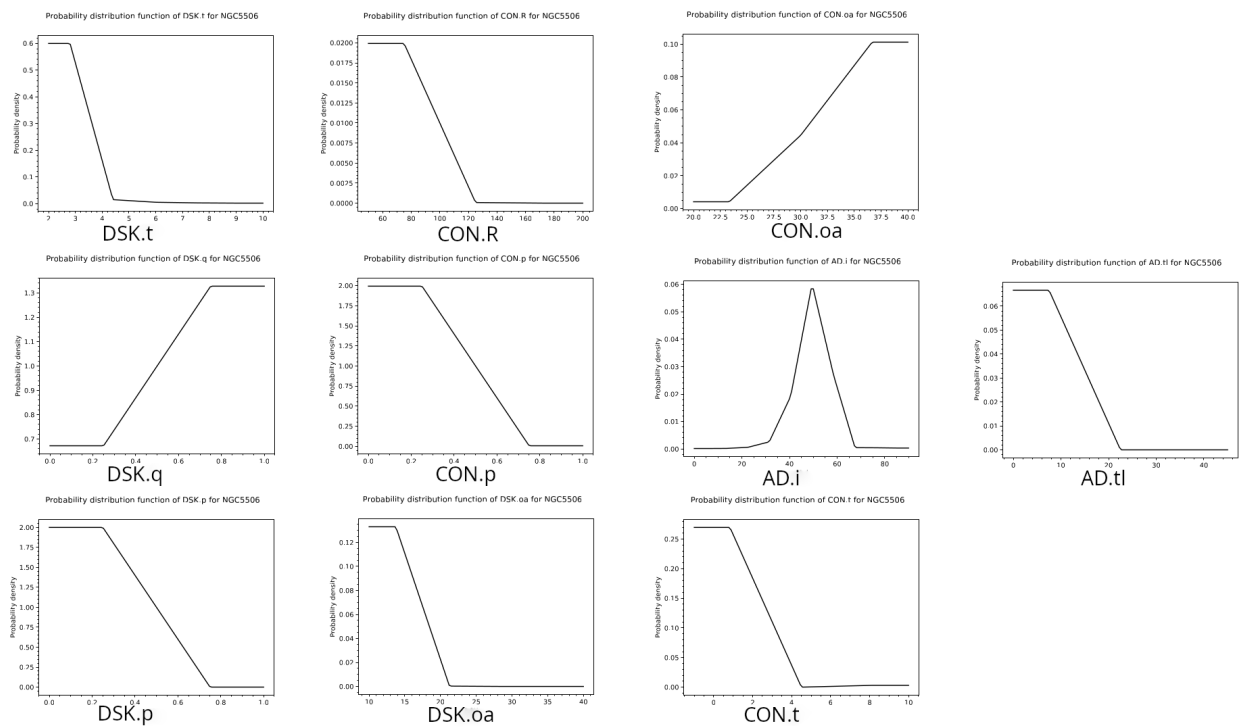


Figure 24: Probability density function plots of parameters with the Disk+cone model for NGC 5506.

Summary

Recent observations of infrared structure from nearby AGNs have revealed that a significant number of them exhibit extended mid-infrared (MIR) polar emissions. This discovery challenges the traditional AGN unification model, which posits a single equatorial dust structure as the source of obscuration, explaining the observed differences between Type-1 and Type-2 AGNs.

Using high-resolution mid-infrared interferometric observations, which resolved structures on sub-parsec scales, two distinct dust components were identified: a thin, disk-like structure and a larger much less dense elongated structure, roughly perpendicular to the disk. This elongated polar structure accounts for around 80% of the $8 - 13\mu\text{m}$ emission. Many studies have suggested that this MIR polar elongation is due to dusty winds driven by radiation pressure.

In this project, we selected three nearby AGNs—ESO 323-77, ESO 428-14, and NGC 5506—that have previously shown evidence of a MIR polar extension. We obtained mid-infrared imaging and spectral data from the VLT VISIR instrument from each of these objects, which we downloaded from the ESO archive and processed using the ESO Reflex pipeline. In addition, L-band imaging data from the ISAAC instrument was acquired and reduced with EsoRex for ESO 323-77.

We derived the spectral energy distributions (SEDs) for all three sources and the binned spectra were then used in SED fitting with CIGALE. Two model libraries were employed for the SED fitting: the clumpy two-phase torus model by Stalevski et al. (2016), and the disk+cone model developed by Božilović (2019), based on the disk+cone model described in Stalevski et al. (2017, 2019); Stalevski et al. (2023).

Comparing the results of the SED fitting with the clumpy two-phase (SKIRTOR) and the disk+cone models, we found that in two of the three selected sources (ESO 428-14 and NGC 5506), the SKIRTOR model provided a better fit to the observed SED. However, in ESO 323-77, the disk+cone model performed better. Notably, the $9.7\mu\text{m}$ silicate absorption feature was not well fitted by the disk+cone model. We suggest that the inability of the new disk+cone model to accurately fit the observed SED may be due to the limited parameter ranges within the model compared to the SKIRTOR library.

Future work will involve expanding the parameter ranges for the disk+cone model and characterizing dusty winds in a larger sample of AGNs.

References

- Antonucci, R. (1993). Unified models for active galactic nuclei and quasars. *Annual Review of Astronomy and Astrophysics*, 31:473–521.
- Asmus, D. (2019). New evidence for the ubiquity of prominent polar dust emission in AGN on tens of parsec scales. *Monthly Notices of the Royal Astronomical Society*, 489(2):2177–2188.
- Asmus, D., Gandhi, P., Hönig, S. F., Smette, A., and Duschl, W. J. (2016). High angular resolution mid-infrared properties of agn: Ii. the emission and structure of the torus. *Monthly Notices of the Royal Astronomical Society*, 463:2879–2902.
- Baes, M. et al. (2010). The skirt radiative transfer code: Dusty discs and dust lanes. *Astronomy & Astrophysics*, 518:L39.
- Bianchi, S., Guainazzi, M., Matt, G., and Fonseca Bonilla, N. (2010). Suzaku and xmm-newton observations of ngc 5506: A heavily obscured seyfert 2. *Monthly Notices of the Royal Astronomical Society*, 407(4):289–297.
- Boquien, M., Burgarella, D., Roehlly, Y., Buat, V., Ciesla, L., Corre, D., Inoue, A. K., and Salas, H. (2019). Cigale: a python code investigating galaxy emission. *Astronomy Astrophysics*, 622:A103.
- Božilović, A. (2019). Vetrovi prašine u aktivnim galaktičkim jezgrima. M.sc. thesis, University of Belgrade.
- Bruzual, G. and Charlot, S. (2003). Stellar population synthesis at the resolution of 2003. *Monthly Notices of the Royal Astronomical Society*, 344(4):1000–1028.
- Calzetti, D., Armus, L., Bohlin, R. C., Kinney, A. L., Koornneef, J., and Storchi-Bergmann, T. (2000). The dust content and opacity of actively star-forming galaxies. *The Astrophysical Journal*, 533(2):682–695.
- Cashwell, E. D. and Everett, C. J. (1959). *A practical manual on the Monte Carlo method for random walk problems*. Pergamon Press.
- Dale, D. A., Helou, G., Magdis, G. E., Armus, L., Díaz-Santos, T., and Shi, Y. (2014). A Two-parameter Model for the Infrared/Submillimeter/Radio Spectral Energy Distributions of Galaxies and Active Galactic Nuclei. *The Astrophysical Journal*, 784(1):83.
- Davies, R. L. et al. (2020). Black hole growth and feedback through cosmic time. *Nature Astronomy*, 4:650–658.

- De Looze, I. et al. (2010). The dust emission of spiral galaxies: A detailed analysis of the fir/submm seds of ngc 891 and ngc 4565. *Astronomy & Astrophysics*, 518:L54.
- Draine, B. T. and Li, A. (2007). Infrared emission from interstellar dust. iv. the silicate-graphite-pah model in the post-spitzer era. *The Astrophysical Journal*, 657(2):810–837.
- Elitzur, M. (2012). *An Introduction to Active Galactic Nuclei*. Cambridge University Press.
- Fabian, A. C. (2012). Observational evidence of active galactic nuclei feedback. *Annual Review of Astronomy and Astrophysics*, 50:455–489.
- Fanaroff, B. L. and Riley, J. M. (1974). The morphology of extragalactic radio sources of high and low luminosity. *Monthly Notices of the Royal Astronomical Society*, 167:31P–36P.
- Ferruit, P., Wilson, A. S., and Mulchaey, J. (2000). Hubble space telescope optical and near-infrared imaging of the active galaxy eso 428-g14. *The Astrophysical Journal Supplement Series*, 128(2):139–164.
- Freudling, W. (2013). Automated data reduction workflows for astronomy: The eso reflex environment. *Astronomy and Astrophysics*, 559.
- Fritz, J., Franceschini, A., and Hatziminaoglou, E. (2006). Revisiting the infrared spectra of active galactic nuclei with a new torus emission model. *Monthly Notices of the Royal Astronomical Society*, 366(3):767–786.
- Ghisellini, G. (2010). The jet/disk connection in blazars. In *American Institute of Physics Conference Series*, volume 1242, pages 43–54.
- Giommi, P., Padovani, P., Polenta, G., Turriziani, S., D’Elia, V., and Piranomonte, S. (2012). A simplified view of blazars: Clearing the fog around long-standing selection effects. *Monthly Notices of the Royal Astronomical Society*, 420:2899–2911.
- Harrison, C. M. (2017). Impact of supermassive black hole growth on star formation. *Nature Astronomy*, 1:0165.
- Heckman, T. M. and Best, P. N. (2014). The co-evolution of galaxies and supermassive black holes: Insights from surveys of the contemporary universe. *Annual Review of Astronomy and Astrophysics*, 52:589–660.

- Ho, L. C. (2008). Nuclear activity in nearby galaxies. *Annual Review of Astronomy and Astrophysics*, 46:475–539.
- Hönig, S. F. (2019). The dusty heart of active galaxies and the black hole-galaxy connection. *The Astrophysical Journal*, 884(2):171.
- Hönig, S. F., Kishimoto, M., Antonucci, R., Marconi, A., Prieto, M. A., Tristram, K., and Weigelt, G. (2012). Parsec-scale Dust Emission from the Polar Region in the Type 2 Nucleus of NGC 424. *The Astrophysical Journal*, 755(2):149.
- Hönig, S. F., Kishimoto, M., Antonucci, R., Marin, F., Stockton, A., Packham, C., Barvainis, R., and Siebenmorgen, R. (2013). Dust in the polar region as a major contributor to the infrared emission of active galactic nuclei. *The Astrophysical Journal*, 771(2):87.
- Hopkins, P. F. et al. (2016). Black holes in galaxies: The formation, fueling, and feedback of supermassive black holes. *Monthly Notices of the Royal Astronomical Society*, 458(4):816–843.
- Hönig, S. F. and Beckert, T. (2007). The dusty torus in active galactic nuclei: The effect of clumpiness on the infrared emission. *The Astrophysical Journal*, 668:128–144.
- Hönig, S. F. and Beckert, T. (2011). The dust distribution in active galactic nuclei and the impact on the infrared emission. *The Astrophysical Journal*, 741(2):73.
- Hönig, S. F. and Kishimoto, M. (2017). The dusty heart of active galaxies: Polar dust and the black hole-galaxy connection. *The Astrophysical Journal*, 837(2):149.
- Jaffe, W., Meisenheimer, K., Schartmann, M., Greenhill, L. J., I., R., T., A., H., , and L. (2004). The circumnuclear dust in the seyfert galaxy ngc 1068. *Nature*, 429:261–263.
- Kewley, L. J. and Nicholls, D. C. (2019). Understanding the excitation mechanisms of optical emission lines in active galaxies. *Annual Review of Astronomy and Astrophysics*, 57:511–570.
- Khachikian, E. Y. and Weedman, D. W. (1974). An atlas of seyfert galaxies. *The Astrophysical Journal Supplement Series*, 27:1–113.
- Krolik, J. H. (1999). *Active Galactic Nuclei: From the Central Black Hole to the Galactic Environment*. Princeton University Press, Princeton, NJ.
- Lagage, P.-O., Pel, J.-W., Authier, M., Belorgey, J., Clédassou, R., Doucet, C., Dubreuil, D., and et al. (2004). Successful commissioning of visir: The mid-infrared vlt instrument. *The Messenger*, 117:12–16.

- Laha, S. and Ghosh, R. (2020). Supermassive black hole feedback in a multiphase medium. *Nature Astronomy*, 4:722–728.
- Laing, R. A., Jenkins, C. R., Wall, J. V., and Unger, S. W. (1994). Spectrophotometry of a complete sample of 3cr radio sources: Implications for unified models. In *The Physics of Active Galaxies*, volume 54, page 201.
- Lawrence, A. (1991). The unified scheme for active galactic nuclei and quasars. *The Astrophysical Journal*, 366:85–93.
- Leftley, J., Gandhi, P., Hönig, S. F., Asmus, D., Nardini, E., Ricci, C., Fini, L., , and J. (2018). New evidence for the dusty wind model: Polar dust and a hot core in the type-1 seyfert eso 323-g77. *The Astrophysical Journal*, 862:17.
- Lusso, E., Hennawi, J. F., Comastri, A., Zamorani, G., Richards, G. T., Vignali, C., Treister, E., Schawinski, K., and Salvato, M. (2013). The x-ray to optical-uv luminosity ratio of quasars is constant at high redshift: The lx-luv relation. *The Astrophysical Journal*, 777(2):86.
- Lyu, J. and Rieke, G. H. (2018). The nature of hot dust: Hot agn dust challenged by hot dust-poor agns. *The Astrophysical Journal*, 866(2):92.
- Maraston, C. (2005). Evolutionary population synthesis: Models, analysis of the ingredients and application to high-z galaxies. *Monthly Notices of the Royal Astronomical Society*, 362(3):799–825.
- Moorwood, A. et al. (1998). Isaac sees first light at the vlt. *The Messenger*, 94:7–9.
- Mulchaey, J. S., Wilson, A. S., and Tsvetanov, Z. (1996). A hubble space telescope imaging survey of the narrow-line regions in seyfert galaxies. *The Astrophysical Journal Supplement Series*, 102:309–340.
- Nenkova, M., E., S., E., , , , and D. (2008). A new model for the clumpy torus in active galactic nuclei. *The Astrophysical Journal*, 685:147–156.
- Netzer, H. (2013). *The physics and evolution of active galactic nuclei*. Cambridge University Press.
- Netzer, H. (2015). Revisiting the unified model of active galactic nuclei. *Annual Review of Astronomy and Astrophysics*, 53:365–408.
- O’Dea, C. P., Baum, S. A., and Stanghellini, C. (1991). What are the gigahertz-peaked spectrum radio sources? *The Astrophysical Journal*, 380:66–77.

- Osterbrock, D. E. (1981). Seyfert galaxies with weak broad h alpha emission lines. *Astrophysical Journal*, 249:462–470.
- Osterbrock, D. E. and Ferland, G. J. (2006). *Astrophysics of Gaseous Nebulae and Active Galactic Nuclei*. University Science Books, Sausalito, CA.
- Osterbrock, D. E. and Pogge, R. W. (1985). The spectra of narrow-line seyfert 1 galaxies. *Astrophysical Journal*, 297:166–176.
- Padovani, P. (2016). The faint radio sky: Radio astronomy becomes mainstream. *Astronomy and Astrophysics Review*, 24:13.
- Padovani, P. (2017). Active galactic nuclei: What’s in a name? *The Astrophysical Journal*, 844(1):36.
- Padovani, P. and Giommi, P. (1995). The connection between x-ray- and radio-selected bl lacertae objects. *Astrophysical Journal*, 444:567–581.
- Peterson, B. M. (1997). *An Introduction to Active Galactic Nuclei*. Cambridge University Press, Cambridge, UK.
- Pooge, S. (2000). New active galactic nucleus observations. *New Astronomy Review*, 44:381–384.
- Ramos Almeida, C. et al. (2011). Nuclear dust properties of powerful radio galaxies and type-2 quasars: An infrared study. *Monthly Notices of the Royal Astronomical Society*, 417(2):2036–2052.
- Ramos Almeida, C. and Ricci, C. (2017). Multiwavelength view of agn obscuration. *Nature Astronomy*, 1:679–689.
- Ricci, C., Bauer, F. E., Arevalo, P., et al. (2016). An x-ray view of the clumpy torus in ngc 1068: the role of the torus in active galactic nuclei. *Monthly Notices of the Royal Astronomical Society*, 456:245–260.
- Ricci, C. et al. (2017). Nuclear obscuration in local active galactic nuclei: An infrared and x-ray perspective. *Monthly Notices of the Royal Astronomical Society*, 468(2):1273–1299.
- Risaliti, G., Young, M., and Elvis, M. (2009). Probing the structure of the x-ray obscurer in ngc 1365 with xmm-newton and chandra. *The Astrophysical Journal*, 700(2):L6–L9.

- Stalevski, M., Asmus, D., and Tristram, K. R. W. (2017). A dusty wind as a torus alternative in the active galactic nucleus of the circinus galaxy. *Monthly Notices of the Royal Astronomical Society*, 472:3854–3870.
- Stalevski, M., Fritz, J., Baes, M., Hosseini, S., Popović, L. v., Gruppioni, C., and Galliano, F. (2016). A new look at the clumpy torus in active galactic nuclei: How important is the polar component? *Monthly Notices of the Royal Astronomical Society*, 458(2):2288–2311.
- Stalevski, M., Fritz, J., Baes, M., Nakos, T., and Popović, L. v. (2012a). 3d radiative transfer modelling of the dusty tori around active galactic nuclei: the effects of clumpiness on the silicate features and the near-infrared emission. *Monthly Notices of the Royal Astronomical Society*, 420:2756–2772.
- Stalevski, M., Fritz, J., Baes, M., Nakos, T., and Popović, L. v. (2012b). Clumpy tori around active galactic nuclei: the effects of clumpiness on the torus sed and the resulting classification of agns. *Monthly Notices of the Royal Astronomical Society*, 419:1855–1874.
- Stalevski, M., González-Gaitán, S., Savić, Đ., Kishimoto, M., Mourão, A., Lopez-Rodríguez, E., and Asmus, D. (2023). Dissecting the active galactic nucleus in Circinus - III. VLT/FORS2 polarimetry confirms dusty cone illuminated by a tilted accretion disc. , 519(3):3237–3256.
- Stalevski, M., Tristram, K. R. W., Asmus, D., Ramos Almeida, C., Buchner, J., and Schnorr-Müller, A. (2019). Torus, polar dust or both? n-band interferometric imaging of the circinus galaxy with matisse. *Monthly Notices of the Royal Astronomical Society*, 484:3334–3350.
- Sulentic, J. W., Marziani, P., and Dultzin-Hacyan, D. (2000). The physics of broad-line active galactic nuclei and their relation to the host galaxies. *Annual Review of Astronomy and Astrophysics*, 38:521–572.
- Tran, H. D. (2001). The unified model and spectropolarimetric observations of seyfert 2 galaxies. *The Astrophysical Journal*, 554(2):L19–L22.
- Tristram, K. R. W., Jaffe, W., Meisenheimer, K., Schartmann, M., Hönic, S. F., , , , , T., and R. (2007). The clumpy torus in the seyfert galaxy ngc 1068. *Astronomy & Astrophysics*, 474:837–845.
- Ulvestad, J. S. and Wilson, A. S. (1989). Radio structures of seyfert galaxies. ii. high-resolution vla observations of 42 sources. *The Astrophysical Journal*, 343:659–670.

- Urry, C. M. and Padovani, P. (1995). Unified schemes for radio-loud active galactic nuclei. *Publications of the Astronomical Society of the Pacific*, 107:803–845.
- Véron-Cetty, M.-P. and Véron, P. (2010). A catalogue of quasars and active nuclei: 13th edition. *Astronomy & Astrophysics*, 518:A10.
- Wada, K. (2015). The effect of agn feedback on the dusty torus. *The Astrophysical Journal*, 808(1):1.
- Weymann, R. J., Carswell, R. F., and Smith, M. G. (1981). Absorption lines in the spectra of quasistellar objects. *Annual Review of Astronomy and Astrophysics*, 19:41–76.
- Wilson, A. S. and Tsvetanov, Z. I. (1994). Ionization cones and radio jets in active galaxies. *The Astronomical Journal*, 107(4):1227–1233.
- Witt, A. N. (1977). Multiple scattering in reflection nebulae. i - a monte carlo approach. *The Astrophysical Journal Supplement Series*, 35:1–6.
- Yang, G., Boquien, M., Buat, V., Burgarella, D., Ciesla, L., Duras, F., Stalevski, M., Brandt, W. N., and Papovich, C. (2020). X-cigale: fitting agn/galaxy seds from x-ray to infrared. *Monthly Notices of the Royal Astronomical Society*, 491(1):740–761.

Appendix

Python Script

This Python script is written for processing reduced imaging and spectral data. Aperture photometry and Gaussian fitting are performed on the images, while the spectra are sigma-clipped, lines are removed, and the spectra are binned in preparation for fitting.

```
#!/usr/bin/env python3
# -*- coding: utf-8 -*-
"""
Created on Fri Apr 19 13:08:21 2024

@author: jfaniyi
"""

#####
#ONLY SED ESO 323
#####

#import Libraries
import numpy as np
from astropy.io import fits
import matplotlib.pyplot as plt
from photutils.aperture import CircularAperture, CircularAnnulus
from photutils.aperture import aperture_photometry, ApertureStats
from glob import glob
from astropy.modeling import models, fitting
from astropy.utils.exceptions import AstropyUserWarning
#ignore warnings in Gaussian fitting
from scipy.signal import medfilt
from datetime import datetime, timedelta
from astropy.stats import sigma_clip
```

```

#adjust parameters for plotting for bigger labels
params = {'legend.fontsize': 'xx-large',
          'figure.titlesize': 'xx-large',
          'figure.subplot.top': 0.93,
          'figure.subplot.wspace': 0.3,
          'figure.figsize': (7,6),
          'axes.labelsize': 'xx-large',
          'axes.titlesize': 'xx-large',
          'xtick.labelsize': 'xx-large',
          'ytick.labelsize': 'xx-large',
          'text.usetex' : True}
plt.rcParams.update(params)

#photometry files, spectroscopy files, and, standard stars===ES0323-77===
fits_files=glob('ES0323spc_2023-10-30T15:54:17/*/*ES0323*.fits') #spc
fits_filess=glob('eso323_spc_rereduced_2024-04-17T19:30:54/*/*ES0323*.fits') #spc
fits_filesss=glob('eso323_spc_rerereduced_2024-04-18T14:12:46/*/*ES0323*.fits')
img_files=glob('ES0323img_2023-11-13T17:09:12/*/*OBJ*.fits')
std_stars=glob('ES0323img_2023-11-13T17:09:12/*/*PHOT*.fits')

#functions
'''define functions to extract the dates, seeing,
and filter name from the header of the photometry data.'''
def extract_mjds(fitsfile):
    with fits.open(fitsfile) as hdul:
        head_r = hdul[0].header
        # Extract the MJD value from the header
        mjd = head_r.get('MJD-OBS', None)
        return mjd
def extract_seeing(fitsfile):
    with fits.open(fitsfile) as hdul:
        header = hdul[0].header
        see = header.get('HIERARCH ESO TEL IA FWHM', None)
        return see

```

```

def extract_filt(fitsfile):
    with fits.open(fitsfile) as hdul:
        header = hdul[0].header
        filt_name = header.get('HIERARCH ESO INS FILT1 NAME', None)
        return filt_name

def remove_spikes(data, threshold=0.2):
    mean = np.mean(data)
    std_dev = np.std(data)
    spikes = np.abs((data - mean) / std_dev)
    data_cleaned = data[spikes < threshold]
    #data_cleaned[spikes] = np.interp(np.where(spikes)[0],
    np.where(~spikes)[0], data[~spikes])
    return data_cleaned

def remove_spikes2(data, window_size=3):
    median_filtered = medfilt(data, kernel_size=window_size)
    cleaned_data = np.where(np.abs(data - median_filtered) > 0.2*np.std(data),
    median_filtered, data)
    return cleaned_data

def remove_nans(array):
    return array[~np.isnan(array)]

def bin_data(x, y, bin_size):
    binned_x = []
    binned_y = []
    stdx=[]
    stdy=[]
    for i in range(0, len(x), bin_size):
        bin_x = np.mean(x[i:i+bin_size])
        bin_x_std=np.std(x[i:i+bin_size])
        bin_y = np.mean(y[i:i+bin_size])
        bin_y_std=np.std(y[i:i+bin_size])
        binned_x.append(bin_x)
        binned_y.append(bin_y)
        stdx.append(bin_x_std)
        stdy.append(bin_y_std)
    return np.array(binned_x), np.array(binned_y),np.array(stdx),np.array(stdy)

def mjd2000_to_ddmmyyyy(mjd2000):
    # Offset between MJD2000 and Unix epoch

```

```

mjd2000_epoch_offset = 40587
# Convert MJD2000 to Unix timestamp (seconds since 1970-01-01 00:00:00 UTC)
unix_timestamp = (mjd2000 - mjd2000_epoch_offset) * 86400
#unix_timestamp = mjd2000 * 86400
# Convert Unix timestamp to datetime object
date = datetime.datetime.utcfromtimestamp(unix_timestamp)
# Format the datetime object as ddmmyyyy
return date.strftime('%d%m%Y')
def remove_edges(flux,size):
    edge_removed= flux[size:-size]
    return edge_removed
def remove_edges_end(flux,a,b):
    edge_removed= flux[a:b]
    return edge_removed

filternames=['M-BAND',
'J7.9', 'PAH1', 'J8.9', 'B8.7', 'ARIII', 'SIV_1', 'B9.7', 'SIV', 'B10.7', 'SIV_2', 'PAH2', 'B11.7',
'PAH2_2', 'J12.2', 'NEII_1', 'B12.4', 'NEII', 'NEII_2', 'Q1', 'Q2', 'Q3']
filt_cen_values=[4.67,7.72,8.58,8.7,8.91,8.98,9.81,9.82,10.47,10.64,10.71,11.24,11.51,
11.68,11.93,12.22,12.45,12.8,13.04,17.65,18.72,19.5]
filt_width=[0.52,0.56,0.41,0.74,0.92,0.14,0.19,0.82,0.17,1.34,0.2,0.54,
0.9,0.37,0.52,0.18,1.03,0.2,0.22,0.83,0.88,0.4]
plt.figure(figsize=(16,9))
wavelengths = []
intensities = []
spc_error=[]
nfluxes=[]
cl_wavelengths=[]
wavelength_edge_removed=[]
nflux_edge_removed=[]
nfluxxes=[]
wavelengthhs=[]
for fits_file in fits_filesss:
    hdulist = fits.open(fits_file) #open SPC_files file
    data = hdulist[1].data
    header = hdulist[1].header

```

```

# Extract wavelength information from the FITS header
intensity = data['SPC_CALIBRATED']*1000000 #converts to units in micrometers
error= data['SPC_CALIBRATED_ERROR']*1000000
wavelength = data['WLEN']*1000000
'''note: variable intenstiy is the flux, and flux is the converted nuFnu'''
cl = 2.998e8
c =cl/wavelength
nflux= c*intensity* 1e-26
wavelength=wavelength[~np.isnan(nflux)]
nflux = remove_nans(nflux)
nfluxes=np.append(nfluxes,nflux)
#remove edges
nflux=remove_edges(nflux,15)
wavelength=remove_edges(wavelength,15)
nflux_edge_removed=np.append(nflux_edge_removed,nflux)
#Append wavelength and intensity data to their respective lists
wavelength_edge_removed=np.append(wavelength_edge_removed, wavelength)
target_wavelengths=[8,13]
ix_to_cut = [np.abs(wavelength - wl).argmin() for wl in target_wavelengths]
nfluxx=remove_edges_end(nflux, ix_to_cut[0], ix_to_cut[1])
wavelengthh=remove_edges_end(wavelength, ix_to_cut[0], ix_to_cut[1])
wavelengthhhs=np.append(wavelengthhhs,wavelengthh)
nfluxxes=np.append(nfluxxes,nfluxx)
#cl_wavelengths=remove_spikes(wavelengths)
#cl_wavelengths=np.append(cl_wavelengths, remove_spikes(wavelengths))
intensities=np.append(intensities, intensity)
spc_error=np.append(spc_error,error)
#mask=(intensity/error)>2.8#
threshold=2
meann = np.mean(nflux)
std_devv = np.std(nflux)
spikess = np.abs((nflux - meann) / std_devv)
data_cleaned = nflux[spikess < threshold]
#mask=remove_spikes(nflux)

#clipped flux
clipped_flux=sigma_clip(nflux, sigma=2.5, maxiters=7)

```

```

target_wavelengths=[8,13]
#arrange and sort
idx=np.argsort(wavelengthhs)
wavelengthhs=wavelengthhs[idx]
nfluxxes=nfluxxes[idx]
plt.plot(wavelengthhs,nfluxxes)
plt.ylabel('$vF_{\nu}$[ergs/s/cm2]$')
plt.ylim(-0.05e-9,3.5e-10)
plt.xlim(7.9,13)
plt.title('SED for ES0323-77')
#plt.show()

idx=np.argsort(wavelengthhs)
wavelengthhs=wavelengthhs[idx]
nfluxxes=nfluxxes[idx]

#nfluxxes=nfluxxes[:,-1]
#nfluxxes=nflux
#wavelengthhs=wavelength
nflux=nfluxxes[:len(nfluxxes)//6 *6]
wavelength=wavelengthhs[:len(wavelengthhs)//6 *6]
nflux=nflux.reshape((6,-1))
nflux_median=np.median(nflux,axis=1)
wavelength=wavelength.reshape((6,-1))
wavelength_median=np.median(wavelength,axis=1)
nflux_std=nflux.reshape((6,-1)).std(axis=1)
#plt.subplot(212)
plt.errorbar(wavelength_median,nflux_median,yerr=nflux_std,fmt='o',
label='binned spectra')

# =====
# plt.grid(which='major', color='#DDDDDD', linewidth=0.8)
# plt.grid(which='minor', color='#EEEEEE', linestyle=':', linewidth=0.5)
# plt.minorticks_on()
# plt.xlabel('Wavelength [microns]')

```

```

# plt.ylabel('$vF_{\nu}$[ergs/s/cm2])')
# plt.ylim(-0.05e-9,3.5e-10)
# plt.xlim(7,13.5)
# =====

phot_bkg_sub=[]
agn_flux = []
host_galaxy_flux = []
mjd_value = []
filt_names = []
see = []
residuals = []
fitted_model_list = []
yerr=[]
dates=[]
fcen=[]

for n,s in enumerate(std_stars):
    '''First fit the standard stars'''
    '''Use 2D-Airy disk + constant'''
    hdulist= fits.open(s)
    data=hdulist[0].data
    brightest = np.unravel_index(np.argmax(data),data.shape)
    positions = [(brightest[1],brightest[0])]
    q,r=np.indices(data.shape)
    initial_guess = (np.max(data)/1.5, np.argmax(data) % data.shape[1],
    np.argmax(data) // data.shape[1], 1.22*2.355*(1.7/8.6)*filt_cen_values[n])
    gaussian = models.AiryDisk2D(*initial_guess) + models.Const2D(0.0002)
    fitter = fitting.LevMarLSQFitter()
    fitted_model = fitter(gaussian, r, q, data, maxiter=10000)
    g_fit = fitted_model(r,q)
    fitted_model_list.append(fitted_model)
    xcenter=int(fitted_model[0].x_0.value)
    ycenter=int(fitted_model[0].y_0.value)
    '''Then use as guess for the image fitting'''

```

```

for n,s in enumerate(std_stars):
    '''First fit the standard stars'''
    '''Use 2D-Airy disk + constant'''
    hdulist= fits.open(s)
    fname=extract_filt(s)
    data=hdulist[0].data
    brightest = np.unravel_index(np.argmax(data),data.shape)
    positions = [(brightest[1],brightest[0])]
    q,r=np.indices(data.shape)
    initial_guess = (np.max(data)/1.5, np.argmax(data) % data.shape[1],
    np.argmax(data) // data.shape[1],
    1.22*2.355*(1.7/8.6)*filt_cen_values[filt_names.index(fname)])
    gaussian = models.AiryDisk2D(*initial_guess) + models.Const2D(0.0002)
    fitter = fitting.LevMarLSQFitter()
    fitted_model = fitter(gaussian, r, q, data, maxiter=10000)
    g_fit = fitted_model(r,q)
    fitted_model_list.append(fitted_model)
    xcenter=int(fitted_model[0].x_0.value)
    ycenter=int(fitted_model[0].y_0.value)
    '''Then use as guess for the image fitting'''

for n,f in enumerate(img_files):
    hdulist= fits.open(f) #open
    data=hdulist[0].data
    errors = hdulist[1]
    error = errors.data #read data and error
    date=extract_mjds(f)
    dates=np.append(dates,date)
    #to choose radius size for the aperture photometry
    pixsize=np.abs(hdulist[0].header['CD1_1'])
    pixsize*=3600
    radsize=1/pixsize
    #####
    #filter names
    #####
    fname=extract_filt(f)
    fcen.append(filt_cen_values[filt_names.index(fname)])

```

```

#####
#aperture photometry
#####
brightest = np.unravel_index(np.argmax(data),data.shape)
positions = [(brightest[1],brightest[0])]
aperture = CircularAperture(positions, r=radsizes)
aperture_bkg = CircularAnnulus(positions, r_in=radsizes*2, r_out=radsizes*3)
ap=aperture[0]
phot_table = aperture_photometry(data, aperture,error=error)
aper_stats = ApertureStats(data, aperture_bkg)
bkg = aper_stats.mean * aperture.area
err=aper_stats.std
phot_bkg_sub= np.append(phot_bkg_sub, phot_table['aperture_sum']-bkg)
filt_names=np.append(filt_names, extract_filt(f))
mjd_value=np.append(mjd_value, extract_mjds(f))
see = np.append(see, extract_seeing(f))
yerr = np.append(yerr,phot_table['aperture_sum_err'])
#####
#Gaussian fitting
#####
q,r=np.indices(data.shape)
'''use guess from the standard stars'''
fitted_model = fitted_model_list[n]
initial_guess = (np.max(data), np.argmax(data) % data.shape[1], np.argmax(data),
data.shape[1],
fitted_model[0].radius.value/(1.22*2.355),fitted_model[0].radius.value/(1.23*2.355),0)
guess2 = (np.max(data)/20, np.argmax(data) % data.shape[1], np.argmax(data)
// data.shape[1], (3.6/8.6)*filt_cen_values[filt_names.index(fname)], (2.9/8.6)
*filt_cen_values[filt_names.index(fname)], 0)
'''either two gaussians or 1 gaussian + constant'''
gaussian2 = models.Gaussian2D(*initial_guess) + models.Const2D(aper_stats.mean[0])
+ models.Gaussian2D(*guess2)
gaussian1 = models.Gaussian2D(*initial_guess) + models.Const2D(aper_stats.mean[0])
fitter = fitting.LevMarLSQFitter()
fitted_model2 = fitter(gaussian2, r, q, data, maxiter=10000,
estimate_jacobian=True,acc=1e-12)

```

```

fitted_model1 = fitter(gaussian1, r, q, data, maxiter=10000,
estimate_jacobian=True,acc=1e-12)
g_fit2 = fitted_model2(r,q)
g_fit1 = fitted_model1(r,q)
#residuals
res_gauss1 = data - g_fit1
res_gauss2 = data - g_fit2
'''do a chi square and Bayesian Information Criterion{BIC} to get the best fit.'''
chi_squared_gauss1 = np.sum(res_gauss1**2/(error**2))
chi_squared_gauss2 = np.sum(res_gauss2**2/(error**2))
deg_of_freedom_gauss1 = len(r.flatten())-len(gaussian1.parameters)
deg_of_freedom_gauss2 = len(r.flatten())-len(gaussian2.parameters)
red_chi_squared_gauss1 = chi_squared_gauss1/deg_of_freedom_gauss1
red_chi_squared_gauss2 = chi_squared_gauss2/deg_of_freedom_gauss2
BIC_gauss1 = len(gaussian1.parameters) * np.log(len(r)) + 2*chi_squared_gauss1
BIC_gauss2 = len(gaussian2.parameters) * np.log(len(r)) + 2*chi_squared_gauss2
#choose the best fir, ie, smaller BIC
if BIC_gauss1 < BIC_gauss2:
    g_fit = g_fit1
else:
    g_fit = g_fit2

if BIC_gauss1 < BIC_gauss2:
    agn_flux = np.append(agn_flux,np.sum(fitted_model1[0](q,r)))
else:
    agn_flux = np.append(agn_flux,np.sum(fitted_model2[0](q,r)))

'''host galaxy flux from 2gaussians'''
host_galaxy_flux = np.append(host_galaxy_flux,np.sum(fitted_model2[2](q,r)))
'''centre from the x-mean and y-mean value from the (first)gaussian'''
xcenter=int(fitted_model2[0].x_mean.value)
ycenter=int(fitted_model2[0].y_mean.value)
# =====
#     date=extract_mjds(f)
#     dates=np.append(dates,date)
# =====

```

```

#plot phot points
ddmmyyyy_array = [mjd2000_to_ddmmyyyy(date) for date in dates]

# =====
# plt.errorbar(filt_cen_values,agn_flux*cl*1e-23/(filt_cen_values*(1e-6)),
#             xerr= filt_width, yerr= yerr*cl*1e-23/(filt_cen_values*(1e-6)),
#             color='red',label='agn flux',linestyle='none',marker='o')
# =====
plt.errorbar(fcen,phot_bkg_sub*cl*1e-23/(np.array(fcen)*(1e-6)),
yerr= yerr*cl*1e-23/(np.array(fcen)*(1e-6)), color='black',label='total flux'
,linestyle='none',marker='o')

plt.errorbar(filt_cen_values,phot_bkg_sub*cl*1e-23/(filt_cen_values*(1e-6)),
xerr= filt_width, yerr= yerr*cl*1e-23/(filt_cen_values*(1e-6)), color='black',
label='aperture phot',linestyle='none',marker='o')
plt.errorbar(fcen,agn_flux*cl*1e-23/(np.array(fcen)*(1e-6)), yerr=
yerr*cl*1e-23/(np.array(fcen)*(1e-6)), color='red',label='agn flux',
linestyle='none',marker='o')

#annotate date
for wav,flu, dat in zip(fcen,agn_flux*cl*1e-23/(np.array(fcen)*(1e-6)),
                        ddmmyyyy_array):
    plt.annotate(dat,xy=(wav,flu),xycoords='data',
                 xytext=(1.5,1.5),
                 textcoords='offset points')
for wav,flu, dat in zip(fcen,phot_bkg_sub*cl*1e-23/(np.array(fcen)*(1e-6)),
                        ddmmyyyy_array):
    plt.annotate(dat,xy=(wav,flu),xycoords='data',
                 xytext=(1.5,1.5),
                 textcoords='offset points')
plt.legend(framealpha=0.5)
plt.show()

```

Table 4: The AGN zoo: list of AGN classes. From Padovani (2017)

Class/Acronym	Meaning	Main properties/reference
Quasar	Quasi-stellar radio source (originally)	Radio detection no longer required
Sey1	Seyfert 1	FWHM 1,000 km s ⁻¹
Sey2	Seyfert 2	FWHM 1,000 km s ⁻¹
QSO	Quasi-stellar object	Quasar-like, non-radio source
QSO2	Quasi-stellar object 2	High power Sey2
RQ AGN	Radio-quiet AGN	see ref. 1
RL AGN	Radio-loud AGN	see ref. 1
Jetted AGN		with strong relativistic jets; see ref. 1
Non-jetted AGN		without strong relativistic jets; see ref. 1
Type 1		Sey1 and quasars
Type 2		Sey2 and QSO2
FR I	Fanaroff-Riley class I radio source	radio core-brightened (ref. 2)
FR II	Fanaroff-Riley class II radio source	radio edge-brightened (ref. 2)
BL Lac	BL Lacertae object	see ref. 3
Blazar	BL Lac and quasar	BL Lacs and FSRQs
BAL	Broad absorption line (quasar)	ref. 4
BLO	Broad-line object	FWHM 1,000 km s ⁻¹
BLAGN	Broad-line AGN	FWHM 1,000 km s ⁻¹
BLRG	Broad-line radio galaxy	RL Sey1
CDQ	Core-dominated quasar	RL AGN, $f_{\text{core}} \geq f_{\text{ext}}$ (same as FSRQ)
CSS	Compact steep spectrum radio source	core dominated, $\alpha_{\text{r}} > 0.5$
CT	Compton-thick	$N_{\text{H}} \geq 1.5 \times 10^{24} \text{ cm}^{-2}$
FR 0	Fanaroff-Riley class 0 radio source	ref. 5
FSRQ	Flat-spectrum radio quasar	RL AGN, $\alpha_{\text{r}} \leq 0.5$
GPS	Gigahertz-peaked radio source	see ref. 6
HBL/HSP	High-energy cutoff BL Lac/blazar	$\nu_{\text{synch peak}} \geq 10^{15} \text{ Hz}$ (ref. 7)
HEG	High-excitation galaxy	ref. 8
HPQ	High polarization quasar	$P_{\text{opt}} \geq 3\%$ (same as FSRQ)
Jet-mode		$L_{\text{kin}} \gg L_{\text{rad}}$ (same as LERG); see ref. 9
IBL/ISP	Intermediate-energy cutoff BL Lac/blazar	$10^{14} \leq \nu_{\text{synch peak}} \leq 10^{15} \text{ Hz}$ (ref. 7)
LINER	Low-ionization nuclear emission-line regions	see ref. 9
LLAGN	Low-luminosity AGN	see ref. 10
LBL/LSP	Low-energy cutoff BL Lac/blazar	$\nu_{\text{synch peak}} < 10^{14} \text{ Hz}$ (ref. 7)
LDQ	Lobe-dominated quasar	RL AGN, $f_{\text{core}} < f_{\text{ext}}$
LEG	Low-excitation galaxy	ref. 8
LPQ	Low polarization quasar	$P_{\text{opt}} < 3\%$
NLAGN	Narrow-line AGN	FWHM 1,000 km s ⁻¹
NLRG	Narrow-line radio galaxy	RL Sey2
NLS1	Narrow-line Seyfert 1	ref. 11
OVV	Optically violently variable (quasar)	(same as FSRQ)
Population A		ref. 12
Population B		ref. 12
Radiative-mode		Seyferts and quasars; see ref. 9
RBL	Radio-selected BL Lac	BL Lac selected in the radio band
Sey1.5	Seyfert 1.5	ref. 13
Sey1.8	Seyfert 1.8	ref. 13
Sey1.9	Seyfert 1.9	ref. 13
SSRQ	Steep-spectrum radio quasar	RL AGN, $\alpha_{\text{r}} > 0.5$
USS	Ultra-steep spectrum source	RL AGN, $\alpha_{\text{r}} > 1.0$
XBL	X-ray-selected BL Lac	BL Lac selected in the X-ray band
XBONG	X-ray bright optically normal galaxy	AGN only in the X-ray band/weak lined AGN

The top part of the table relates to major/classical classes. The last column describes the main properties.

When these are too complex, it gives a reference to the first paper, which defined the relevant class or, when preceded by “see”, a recent paper, which gives up-to-date details on it. Reference key: 1. Padovani (2016);

2. Fanaroff and Riley (1974); 3. Giommi et al. (2012); 4. Weymann et al. (1981);

5. Ghisellini (2010); 6. O’Dea et al. (1991); 7. Padovani and Giommi (1995);

8. Laing et al. (1994); 9. Heckman and Best (2014); 10. Ho (2008); 11. Osterbrock and Pogge (1985);

12. Sulentic et al. (2000); 13. Osterbrock (1981)

Biography

Josiah Faniyi was born on 12th of December 1997 in Nigeria. He studied physics at the University of Ibadan, one of the foremost Universities in Nigeria, and is currently completing his Master's degree Astrophysics and Space Science at the University of Belgrade. His research focuses on the infrared study of Active Galactic Nuclei (AGN).

Outside of his research, Josiah is also a dedicated learner of the Serbian language and a lover of Astronomy education and outreaches reflecting his commitment to engaging with diverse cultures and communities. As he looks towards the future, Josiah aspires to pursue a Ph.D. programme where he can continue investigating the mysteries of the universe, particularly focussing on the spectroscopic and photometric study of galaxies, stars, and their environments.